The Thermodynamics of Multifluid Magnetohydrodynamic Turbulence in Star Forming Regions

Aaron Kinsella
B.Sc.

A thesis submitted for the degree of Master of Science

Dublin City University

Supervisor:
Prof. Turlough Downes
School of Mathematical Sciences
Dublin City University

September 2017

Declaration

I hereby certify that this material, which I now submit for assessment of the programme of study leading the the award of Master of Science is entirely my own work, that I have exercised reasonable care to ensure that the work is original, and does not to the best of my knowledge breach any law of copyright, and has not been taken from the work of others save and to the extent that such work has been cited and acknowledged within the text of my work.

Signed:_____

ID Number: 10350697

Date: 7th September 2017

Acknowledgements

There are a number of people I would like to thank for their help and support in completing this work.

First of all I would like to thank my supervisor, Prof. Turlough Downes, for all of his support and guidance throughout the course of this work.

I would also like to thank all of the staff and postgraduate student in the School of Mathematical Sciences, DCU, for all of the interesting discussions and advice over the years. Also, Anita Brady-Boyd and Muhammad Alli for all of the coffee and lunch breaks which helped to keep me sane.

Thank you also to all of my family and friends whose help and encouragement helped to keep me focused when things got difficult, particularly my mother and father, Sharon and Les Kinsella.

A special thank you to Tyler Phillips who has stood by me over the years lending emotional support and helping to keep me motivated.

I would like to thank The Irish Research Council for awarding me the Government of Ireland Scholarship without which this work would not exist and The Irish Centre for High-End Computing (ICHEC) for providing computational resources to run various simulations.

Finally, I would like to dedicate this thesis to my grandmother, Eva Douglas, who sadly passed away during the course of this work.

Contents

1 Introduction **1**
- 1.1 Molecular Clouds . . . 2
  - 1.1.1 Properties of Molecular Clouds . . . 2
  - 1.1.2 Structure of Molecular Clouds . . . 7
- 1.2 Magnetohydrodynamics . . . 22
  - 1.2.1 The Magnetohydrodynamic Equations . . . 22
  - 1.2.2 A Shift to Multifluid MHD . . . 27
  - 1.2.3 Generalised Ohm's Law . . . 29

2 Turbulence in Molecular Clouds **37**
- 2.1 Hydrodynamic Turbulence . . . 37
  - 2.1.1 Turbulent Scales . . . 39
  - 2.1.2 The Kolmogorov Energy Spectrum . . . 39
  - 2.1.3 MHD Turbulence . . . 44
- 2.2 Energy Dissipation in MHD Turbulence . . . 53
  - 2.2.1 Magnetic Heating . . . 53
  - 2.2.2 Current Sheets . . . 55

3 Numerical Methods **59**
- 3.1 HYDRA Code . . . 60
  - 3.1.1 Multifluid MHD Equations . . . 60
  - 3.1.2 Solving The Multifluid MHD Equations . . . 62
  - 3.1.3 Treatment of Magnetic Divergence . . . 73
  - 3.1.4 Shock-Tube Tests . . . 74

4 Results and Discussion **81**
- 4.1 Simulation Set-up . . . 81
  - 4.1.1 Initial Conditions . . . 82
- 4.2 Ideal MHD Turbulence . . . 83
  - 4.2.1 Evolution of Ideal MHD Turbulence . . . 83
  - 4.2.2 Dissipative Structure Identification . . . 84

4.2.3 Dissipation Structures 88
4.3 Multifluid MHD Turbulence 92
4.3.1 Dissipation Structures 92

5 Conclusions **99**

List of Figures

1.1 The path of particle in a magnetic field and its gyroradius . . 17

2.1 Diagram of the turbulent energy cascade showing that energy is transferred from large scales to smaller scales 40
2.2 Schematic energy spectrum for turbulent cascade. It can be seen that in the dissipative range the energy distribution drops of steeply, where as more energy is found at the driving length-scale. (image from:Berselli (2005)) 41
2.3 Illustration of the formation of a current sheet. Magnetic field lines are pushed close together, plasma flows into the current sheet perpendicular to the magnetic field lines at velocity V_{in}, undergoes a velocity increase and flows out of the current sheet in the direction parallel and anti-parallel to field lines at velocity V_{out}. (Image obtained from: Treumann and Baumjohann (2013)) 56
2.4 Basic principle of magnetic reconnection. 56

3.1 The y-component of the magnetic field is shown as well as the x-component of the neutral fluid velocity for case 1 at $h = 5 \times 10^{-3}$ the solution from the dynamic code is shown as points. The overplotted line shows the solution of the steady state equations.(Images taken from O'Sullivan and Downes (2007)) 76
3.2 The x-component of the neutral fluid velocity for case 2 at $h = 2 \times 10^{-3}$ the solution from the dynamic code is shown as points. The overplotted line shows the solution of the steady state equations.(Images taken from O'Sullivan and Downes (2007)) 78

3.3 The y-component of the magnetic field is shown as well as the x-component of the neutral fluid velocity for case 3 at $h = 1 \times 10^{-3}$ the solution from the dynamic code is shown as points. The overplotted line shows the solution of the steady state equations.(Images taken from O'Sullivan and Downes (2007)) 79
3.4 The x-component of the negatively charged fluid species is shown at $h = 1 \times 10^{-3}$. The solution from the dynamic code is shown as points. The overplotted line shows the solution of the steady state equations.(Image taken from O'Sullivan and Downes (2007)) 80

4.1 Evolution of Ideal MHD dissipative structures. 85
4.2 Evolution of the power-law index over time at the start of the simulation (a) and when the simulation had reached a statistical steady state (b) for the case of ideal MHD turbulence. It can be seen that although the initial driving of the turbulence creates large scale structures, the turbulent energy cascade dissipates energy into smaller scale structures. 86
4.3 Visualisation of the current density at $t = 0.3t_c$ for ideal MHD turbulence. It can be seen that dissipative structures of various length-scales are present. 90
4.4 Visualisation of the cross-section of the current density in simulation domain for ideal MHD turbulence at $y = 0.5$. A cross-section of the dissipative structures can be seen. 91
4.5 Plot of the probability distribution of energy dissipation rates for ideal MHD turbulence which is shown by the solid line (P). The index of this power-law is found to be -2.0. The dot-dashed line (Index) is the straight line fit to the power-law tail of the probability distribution, the slope of which is equal to the power law index 91
4.6 Plot of dissipation structures in multifluid MHD turbulence. It can be seen that structures of large length-scales are dominant. 94
4.7 Cross-section of the simulation domain for multifluid MHD turbulence at $y = 0.5$. A cross-section of the dissipative structures can be seen. 95

4.8 Plot of the probability distribution of energy dissipation rates for multifluid MHD turbulence which is shown by the solid line (P) The index of this power-law is found to be -1.02. The dot-dashed line (Index) is the linear fit to the power-law of the probability distribution the slope of which is equal to the power law index (-1.02) 95
4.9 Evolution of the power-law index over $t = [0.1, 0.215]$ sound crossing times for multifluid MHD turbulence. 96
4.10 Evolution of the power-law index over $t = [0.055, 0.215]$ sound crossing times for multifluid MHD turbulence. 96

Abstract

The Thermodynamics of Multifluid Magnetohydrodynamic Turbulence in Star Forming Regions

Aaron Kinsella

It is believed that turbulence is an important process in the evolution and dynamics of molecular clouds and can significantly impact the processes of star formation inside these clouds.
The aim of this project is to investigate the properties of multifluid magnetohydrodynamic turbulence in weakly ionised astrophysical plasmas such as molecular clouds. To do this the formation of structures through which energy can be dissipated, identified primarily by the structures of high current density, will be studied. Ambipolar diffusion dominated systems will be studied with a view to discovering the impact this effect has on the formation of structures and magnetic field topology. The resulting statistics on dissipative structure formation will be compared with ideal MHD simulations. The formation of sheet-like structures is thought to be intrinsic to systems such as those outlined above, so a better understanding of the physical processes involved is a stepping stone in the development of better models for the early phases of star formation.

Chapter 1

Introduction

We present a study of multifluid magnetohydrodynamic turbulence in star forming regions. The regions in which stars form are relatively dense areas of the interstellar medium (ISM) known as molecular clouds. Molecular clouds are made up of weakly ionised plasma and dust, as the material in molecular clouds is weakly ionised it cannot be modelled using the ideal MHD approach. The presence of multiple charged and neutral particle species means that multifluid MHD must be used to describe the fluid.

The following sections of Chapter 1 of this thesis provide an overview of the current literature dealing with molecular clouds, it also discusses the theory of ideal MHD before going on to extend the theory to include multifluid effects.
In Chapter 2 the theory of turbulence in molecular clouds, with particular focus on the mechanisms through which energy is dissipated from turbulent clouds, will be discussed.
A discussion of the numerical method used in this project, including the details of the multifluid MHD code used to run simulations, will be presented in Chapter 3.
The results obtained from a series of simulations will be presented and discussed in Chapter 4.
Finally, Chapter 5 will conclude this thesis, summarising the findings of this

study and suggesting some areas of potential further study.

1.1 Molecular Clouds

The range of sizes of molecular clouds is substantial, they can vary from small clouds of about 1pc across, known as Bok gobules, to giant molecular clouds which can be up to hundreds of parsecs in diameter. Giant molecular clouds contain a large amount of gas and dust, the mass of which can be as much as $10^6 M_\odot$(Sanders et al., 1985).

1.1.1 Properties of Molecular Clouds

General Molecular Cloud Properties

It has been observed both locally, in The Milky Way, and in neighbouring spiral galaxies that most of the molecular gas is concentrated in clumps in the spiral arms of these galaxies. These clouds are believed to be relatively short lived, transient structures with lifetimes believed to be in the order of 30 Myr. Based on observations of the Large Magellanic Cloud by Blitz et al. (2007) the lifespan of a typical molecular cloud can be divided into three main phases.

1. No high mass star formation: this stage of a cloud's life is estimated to last only about 6-7 Myr.

2. *HII* Regions: Due to the observation of two times as many clouds with active *HII* regions than inactive clouds it was estimated that the molecular cloud spends around 14-15 Myr in this stage of its life.

3. Cluster Formation: It is estimated that from the formation of a star cluster to total destruction of the molecular it cloud it takes approximately 6-7 Myr. Stellar winds and outflows from young stellar objects cause material in the molecular cloud to be swept away thereby destroying the cloud in which the cluster is formed.

Molecular clouds are very inhomogeneous regions of the ISM and as such it is difficult to get an accurate idea of the typical densities of giant molecular clouds, for example according to Mac Low and Klessen (2004) clumps in giant molecular clouds can be as dense as $n_H = 10^5 cm^{-3}$ where as Carpenter and Sanders (1998) have observed a cloud (W51) with $n_H = 40 cm^{-3}$, showing the huge variation in the density of gas in molecular clouds.

As the density of gas varies considerably from cloud to cloud, so too does the ionisation fraction vary greatly from cloud to cloud. The ionisation fraction (χ) is the ratio of charged particles to neutral particles in a system, in the case of molecular clouds it is generally the ratio of the number density of electrons to the number density of neutral hydrogen atoms. As stated previously, molecular clouds are primarily composed of hydrogen which has a single electron. If we know the number density of ionised hydrogen atoms then it follows that we know the number density of electrons in the molecular cloud. Then dividing the number density of electrons by the number density of neutral hydrogen, we can find the fraction of atoms in the cloud which are ionised. The ionisation fraction is defined as $\chi \equiv \frac{n_e}{n_H}$ In the previous expression, the number density of neutral hydrogen atoms is given by $n_H = n(H) + 2n(H_2)$. This is obtained quite trivially as $n(H)$ is the number density of neutral hydrogen atoms in the cloud and $n(H_2)$ is the number density of hydrogen molecules in the cloud. As molecular hydrogen is comprised of two hydrogen atoms the total number density of hydrogen atoms in the cloud can be obtained by adding the number density of hydrogen atoms to two times the number density of hydrogen molecules. For optically thin clouds, i.e. clouds with a relatively low density of particles, ambient ultraviolet light from nearby stars or shocks in molecular cloud itself acts to dissociate the electrons from the hydrogen atoms, thus causing the ionisation fraction to increase, typical values for the ionisation fraction in optically thin clouds is $\chi = 10^{-4}$ (Draine et al., 1983, Guelin et al., 1977, Elmegreen, 1979). The ionisation fraction can be measured using indirect determinations of electron abundance. This is done by observing molecular ions and applying various chemical models. The comparison of DCO^+ and HCO^+ is commonly used to

determine the electron abundance in a cloud. For the case of optically thick clouds, i.e. clouds with relatively large densities $n_H \approx 10^4 cm^{-3}$ or greater, hydrogen atoms deep within the cloud are shielded from the ionising effects of UV radiation and as such these clouds have much lower ionisation fractions. The ionisation fraction for dense clouds is in the order of $\chi = 10^{-7}$(Draine et al., 1983, Guelin et al., 1977).

Magnetic Field Observations

As stated previously, it is believed that magnetic fields have an important role to play in the evolution of molecular clouds into protostars. According to Crutcher (1999) the effects of magnetic fields in interstellar clouds cannot be ignored for a number of reasons, such as, the thermal kinetic energy and the magnetic energy in the observed clouds are approximately equal which suggests that MHD waves and static magnetic fields are of equal importance to the energetics of molecular clouds. Also, the ratio of the thermal pressure to the magnetic pressure is less than unity with $\beta_p = 0.4$, where $\beta_p = 2(m_A/M_s)^2$. In the previous expression m_A is the Alfvénic Mach number and M_s is the sonic Mach number. Having a $\beta_p < 1$ indicates that the magnetic pressure dominates the thermal pressure and so magnetic fields are important in molecular cloud evolution (Crutcher, 1999).

It is possible to determine the strength of a magnetic field using the Zeeman effect. However the often complex morphology of the magnetic field in molecular clouds leads to the variation of field strength within the cloud. According to observations by Crutcher (1999), the median field strength of clouds in his sample was $\bar{B}_{med} = 20\mu$G and the average value of the magnetic field strength was $\bar{B} = 7.6\mu$G. Observations by Troland (2005) have determined that the strength of the median magnetic field of the diffuse interstellar medium to be $\bar{B}_{med} = 6\mu$G.

An important parameter when discussing the effects of magnetic fields on molecular clouds is the ratio of mass to magnetic flux, M/ϕ_B. The mass-to-

flux ratio is useful in determining the ability of a magnetic field to support a cloud from collapsing under self-gravity. Clouds with a mass-to-flux ratio below a critical value are said to be subcritical and is magnetostatically stable. Clouds with a mass-to-flux ratio above a critical value are said to be supercritical and susceptible to gravitational collapse (Mac Low and Klessen, 2004). The critical mass of a cloud in the presence of a magnetic field can be derived as follows from Mac Low and Klessen (2004).

If it is assumed that all surface terms except pressure P_0 are negligible and the magnetic field is uniform through a spherical cloud of radius R and density ρ then the virial equation is given by;

$$4\pi R^3 P_0 = 3\frac{Mk_BT}{\mu} - \frac{1}{R}\left(\frac{3}{5}GM^2 - \frac{1}{3}R^4B^2\right) \tag{1.1}$$

Where k_B is Boltzmann's constant, T is the temperature of the cloud, and μ is the mean mass per particle. M is the mass of the region and is given by;

$$M = \frac{4}{3}\pi R^3 \rho \tag{1.2}$$

The magnetic flux Φ is given by;

$$\Phi = \pi R^2 B \tag{1.3}$$

If the radius is rewritten in terms of the mass and density then it is pos-

sible to find the critical mass at which gravitational collapse will over come the magnetic support;

$$M_{cr} = \frac{5^{3/2}}{48\pi^2}\frac{B^3}{G^{3/2}\rho^2} \tag{1.4}$$

The critical mass can then be written in terms of the critical value for the mass-to-flux ratio as noted by Mouschovias and Spitzer (1976), Mouschovias (1976) and is given as;

$$\left(\frac{M}{\Phi}\right)_{cr} = \frac{\zeta}{3\pi}\left(\frac{5}{G}\right)^{1/2} \tag{1.5}$$

Where M is the mass of the cloud, ϕ is the magnetic flux and $\zeta = 0.5$ for a uniform sphere gives a critical mass-to-flux as $(M/\phi)_{cr} = 490\,\mathrm{g}G^{-1}cm^{-2}$. Observations have found that the majority of clouds are supercritical and as such, susceptible to gravitational collapse. For clouds with extremely large magnetic field strengths parts of the cloud may be subcritical. As neutral particles are not directly affected by the magnetic field and can slip past the field lines and charged particles the cores of such clouds can quickly become supercritical and collapse under self-gravity.

Turbulent Support and Driving

It is believed that molecular clouds are turbulent systems. This turbulence can have a significant impact on the on the dynamics of the cloud and therefore may be important in understanding the evolution of the molecular clouds and on the formation of stars in these clouds. It is thought that turbulence may slow down the rate of star formation in molecular clouds. Turbulent motions in the cloud can act to stir up the material present in the cloud so regions of high density in the cloud where gravitational collapse could occur may be destroyed by this turbulence and so star formation will not be global and will be quite inefficient. If the turbulence is supersonic star formation

can be halted completely as the dense regions are not given enough time to become supercritical (Mac Low and Klessen, 2004). In order for turbulence to be present in molecular clouds a driving mechanism must inject energy into the system to drive the turbulent motion. The injection of this energy into the system is not homogeneous or uniform but spans a wide variety of scales. Mac Low and Klessen (2004) argues that the dominant driving mechanisms for supersonic turbulence are supernovae explosions, although the scale at which the shock waves from these explosions contribute to the turbulence is unclear. Another driving mechanism for turbulent motions is the stellar wind from stars in the neighbourhood of the molecular cloud or young stellar objects embedded in the cloud itself. In three dimensions turbulence acts to dissipate the energy which is injected into the system. The turbulence transfers energy from the large scales at which it is injected into the cloud by the driving mechanism to scales at which is can be dissipated through viscous forces. There are a number of mechanisms through which energy can be dissipated in a turbulent cloud including, shocks, vortices and current sheets. A much more in-depth discussion of turbulence and the dissipation processes involved in turbulent clouds can be found in Chapter 2 of this thesis.

1.1.2 Structure of Molecular Clouds

The vast majority of Galactic star formation takes place in giant molecular clouds. The Milky way contains thousands of giant molecular clouds, an example of one such molecular cloud is The Orion molecular cloud located $\approx$ 450pc from Earth. Giant molecular clouds are not homogeneous structures, but have been observed to contain internal small structures, such as clumps and filaments. These clumps are generally a few parsecs across and contain as much as $10^4 M_{\odot}$. It is inside these clumps, in areas known as cloud cores, where star formation is believed to take place. The density of material in the cloud core is even more dense than that of the clump.

Observations of dark clouds in The Galaxy have identified a number of

dense cores, half of which have associated protostars. The other half are thought to be in the pre-stellar phase due to the very narrow line widths observed in these cores. The line widths are similar to those one would expect from thermal broadening suggesting that they are in the early stages of collapse. Comparing the line widths of cloud cores which have an associated protostellar object and starless cores, it is observed that starless cores have narrower line widths suggesting that feedback from prestellar objects creates a turbulent component which broadens the line widths of the cores with which they are associated (Mac Low and Klessen, 2004). The temperature of the core plays a role in the mass of the star that is formed. Cold cores have temperatures of about 10K and have masses of approximately 1 - 10 $M_{\odot}$, the stars formed from these clouds have masses of 1 $M_{\odot}$ or lower. Warm cores generally have temperatures of around 20 - 100K and contain 10 to 1000 $M_{\odot}$ of material, the stars formed from warm clouds are generally more massive than those formed from cold cores (Larson, 2002).

The process of star formation begins when a cloud core starts to undergo gravitational collapse, that is when the force exerted by gravity is greater than all of the other forces, such as gas pressure, that oppose it. Only clouds which meet a certain set of criteria are susceptible to undergo this gravitational collapse. The criteria was first set out by Sir James Jeans, in 1902 (Jeans, 1902), in his work Jeans found that whether or not a cloud would collapse depended on a number of cloud properties, such as the size, temperature and mass of the cloud.

One of the pieces of information which determines if a cloud core is likely to collapse is the Jeans length, this is the length at which the gas cloud is in hydrostatic equilibrium, i.e. not expanding or collapsing. This length scale may be derived quite easily with use of the virial theorem and by ignoring a number of forces such as; rotational forces, magnetic pressure, surface forces, and all external forces. It must also be assumed that the cloud is spherical and the particles have a uniform distribution of mass.

The virial theorem states then that a spherical cloud will be in a state of equilibrium when the time-averaged potential energy ($< U >$) is twice the

time-averaged kinetic energy ($< K >$) contained in the cloud.

$$< K >= - < U > /2 \tag{1.6}$$

In order to derive the expression in equation (1.6) using the approach taken by Binney and Tremaine (2008), we must start with the momentum equation;

$$\frac{\partial(\rho\langle v_j\rangle)}{\partial t} + \frac{\partial(\rho\langle v_i v_i\rangle)}{\partial x_i} + \rho\frac{\partial\Phi}{\partial x_j} = 0 \tag{1.7}$$

Then, multiplying all of the terms in equation (1.7) by x_k and integrating over the volume yields;

$$\frac{\partial}{\partial t}\int \rho x_k\langle v_j\rangle d^3\mathbf{x} = -\int x_k\frac{\partial(\rho\langle v_i v_j\rangle)}{\partial x_i}d^3\mathbf{x} - \int \rho x_k\frac{\partial\Phi}{\partial x_i}d^3\mathbf{x} \tag{1.8}$$

Integrating the first term on the right-hand-side of equation (1.8) by parts gives;

$$\int x_k\frac{\partial(\rho\langle v_i vj\rangle)}{\partial x_i}d^3\mathbf{x} = \int \frac{\partial(\rho x_k\langle v_i v_j\rangle)}{\partial x_i}d^3\mathbf{x} - \int \rho\langle v_i vj\rangle\frac{\partial x_k}{\partial x_i}d^3bfx \tag{1.9}$$

$$= -\int \partial_{ki}\rho\langle v_i v_j\rangle d^3\mathbf{x} \tag{1.10}$$

$$= -\int \langle \upsilon_k \upsilon j \rangle d^3\mathbf{x} \tag{1.11}$$

$$= -2K_{kj} \tag{1.12}$$

where,

$$K_{kj} = \frac{1}{2}\int \rho \langle \upsilon_i \upsilon_j \rangle d^3\mathbf{x} \tag{1.13}$$

is the kinetic-energy tensor. The kinetic-energy tensor can be split into contributions from random and ordered motions as follows;

$$K_{ij} = T_{ij} + \frac{1}{2}\Pi_{ij} \tag{1.14}$$

where;

$$T_{ij} = \frac{1}{2}\int \rho \langle \upsilon_i \rangle \langle \upsilon_j \rangle d^3\mathbf{x} \tag{1.15}$$

and,

$$\Pi_{ij} = \int \rho \sigma_{ij}^2 d^3\mathbf{x} \tag{1.16}$$

The second term on the right-hand-side of equation (1.8) is the potential-energy tensor (U_{ij}).

$$W_{ij} \equiv -\int \rho x_i \frac{\partial \Phi}{\partial x_j} d^3\mathbf{x} \tag{1.17}$$

So, we can write;

$$\frac{\partial}{\partial t} \int \rho x_k \langle \upsilon_j \rangle d^3\mathbf{x} = 2K_{kj} + U_{kj} \tag{1.18}$$

which then allows us to write;

$$\frac{1}{2}\frac{d}{dt} \int \rho [x_k \langle \upsilon_j \rangle + \langle \upsilon_k \rangle] = 2K_{jk} + W_{jk} \tag{1.19}$$

where symmetry is assumed, which allows for the changing of indices.

Next, we define the moment of inertia tensor (I_{ij}) as;

$$I_{ij} = \int \rho x_i x_j d^3\mathbf{x} \tag{1.20}$$

differentiating w.r.t time and utilising the continuity equation results in;

$$\frac{dI_{jk}}{dt} = \int \frac{\partial \rho}{\partial t} x_j x_k d^3\mathbf{x} \tag{1.21}$$

$$= -\int \frac{\partial \rho \langle \upsilon_i \rangle}{\partial x_i} x_j x_k d^3\mathbf{x} \tag{1.22}$$

$$= -\int \frac{\partial (\rho \langle \upsilon_i \rangle x_j x_k)}{\partial x_i} d^3\mathbf{x} + \int \rho \langle \upsilon \rangle \frac{\partial (x_j x_k)}{\partial x_i} d^3\mathbf{x} \tag{1.23}$$

$$= \int \rho \langle \upsilon_i \rangle [x_j \delta_{ik} + x_k \delta_{ij}] d^3\mathbf{x} \tag{1.24}$$

$$= \int \rho [x_j \langle \upsilon_k \rangle + x_k \langle \upsilon_j \rangle] d^3\mathbf{x} \tag{1.25}$$

so;

$$\frac{1}{2}\frac{d}{dt}\int \rho [x_k \langle \upsilon_j \rangle + x_j \langle \upsilon_k \rangle] = \frac{1}{2}\frac{d^2 I_{jk}}{dt^2} \tag{1.26}$$

We can now write the tensor virial theorem as;

$$\frac{1}{2}\frac{d^2 I_{jk}}{dt^2} = 2T_{ij} + \Pi_{ij} + W_{ij} \tag{1.27}$$

This equation,(1.27), relates the gross kinematic and morphological properties of self-gravitating systems.

Next the scalar virial theorem will be derived. Assuming that the system is in a steady state then the moment of inertial tensor will be stationary allowing us to simplify equation (1.27) to;

$$2K_{ij} + W_{ij} = 0 \tag{1.28}$$

Taking the trace of the potential-energy tensor results in the total potential energy of the system, given by;

$$tr(W) = U = \frac{1}{2}\int \rho(\mathbf{x})\Phi(\mathbf{x})d^3\mathbf{x} \tag{1.29}$$

Similarly, the trace of the kinetic-energy tensor results in the total kinetic energy of the system, given by;

$$tr(K) = \sum_{i=1}^{3} K_{ii} = \frac{1}{2}\int \rho(\mathbf{x})[\langle v_1^2\rangle(\mathbf{x}) + \langle v_2^2\rangle(\mathbf{x}) + \langle v_3^2\rangle(\mathbf{x})]d^3\mathbf{x} \tag{1.30}$$

$$= \frac{1}{2}\int \rho(\mathbf{x})\langle v^2\rangle(\mathbf{x})d^3\mathbf{x} \tag{1.31}$$

$$= \frac{1}{2}M\langle v^2\rangle = K \tag{1.32}$$

Thus, we obtain the scalar virial theorem;

$$2K + U = 0 \tag{1.33}$$

or

$$K = -\frac{U}{2} \tag{1.34}$$

Expressions for the time-averaged total potential energy and the time-averaged total thermal kinetic energy must be derived in order to derive the Jeans length. Using the assumption of a spherical cloud of radius (R) with a uniform mass distribution and the above energy balance, this can be done. The average kinetic energy of a particle in a monatomic gas is $\frac{3}{2}K_BT$. Thus, time averages of the kinetic and potential energy can be replaced by the total energies.

$$< K >= K \text{ and } < U >= U \tag{1.35}$$

The total potential energy is then given by;

$$U = \frac{3GM^2}{5R} \tag{1.36}$$

Where G is the gravitational constant and m is the total mass of the cloud. Similarly the total kinetic energy is given by;

$$K = \frac{3}{2}NkT = \frac{3MkT}{m} \tag{1.37}$$

Where N is the number of molecules, k is the Boltzmann constant, T is the temperature and m is the molecular mass.

Substituting equations 1.36 and 1.37 into equation 1.35 and rearranging gives;

$$\frac{GM}{5R} = \frac{kT}{m} \tag{1.38}$$

But since we know the mass of a sphere with uniform mass distribution;

$$M = \frac{4}{3}\pi R^3 \rho \tag{1.39}$$

Where ρ is the mass density of the cloud, using this with equation 1.37 and solving for R gives the Jeans length as;

$$R = \sqrt{\frac{15kT}{4\pi\rho G m}} = \lambda_j \tag{1.40}$$

Where λ_j is the Jeans length, this gives a lower limit for the radius of a cloud, if the clouds radius is above the Jeans length it becomes susceptible to gravitational collapse.

Using the Jeans length it is possible to find the mass at which a cloud or Jeans length in radius is susceptible to collapse, this is known as the Jeans mass and is given by;

$$M_j = \frac{4}{3}\pi\rho\lambda_j \tag{1.41}$$

The Jeans mass gives an upper limit to the mass contained in a cloud which has a radius equal to the Jeans length, if the mass of the cloud is above this critical value it will become gravitationally unstable and collapse. Although the above mechanism for collapse is well understood it does not account for the star formation rates which we observe in the Galaxy. If all clouds above the Jeans mass went into free-fall collapse, the rate of star formation we should observe would be dramatically higher (Mouschovias, 1976). Therefore, other forces must be acting within the cloud slowing down the collapse process, magnetic fields are believed to provide magnetic support which may help retard the collapse of molecular clouds.

Magnetic fields affect the motion of both charged and neutral particles within a molecular cloud. The motion of the charged particles in the molecular cloud is influenced by the Lorentz force;

$$\mathbf{F} = q\mathbf{v} \times \mathbf{B} \tag{1.42}$$

Equation 1.42 for the Lorentz force states that the force experienced by a charged particle is proportional to its velocity and that it acts in a direction that is perpendicular to both the velocity vector and the direction of the magnetic field lines. Charged particles in the presence of magnetic field lines are tied to the lines and only move along those lines but not cross them.
The motion of a charged particle along a magnetic field line is dependent on the magnitude and sign of the charge of the particle also. The magnitude of the charge on the particle determines how strong the force exerted on the particle and therefore how "tightly" it travels around the field line (Young and Freedman, 2012), this is the called the gyroradius (r_g) which is defined as;

$$r_g = \frac{m\nu}{|q|B} \tag{1.43}$$

Where m is the mass of the particle, ν is the velocity, $|q|$ is the magnitude of the charge on the particle and B is the magnetic field. If a particle has a large charge the gyroradius will be small, and if a particle has a small charge the gyroradius will be large, this can be seen in figure 1.1a. The sign of the charge on the particle determines the handedness of the particle's circular path around the field lines (Young and Freedman, 2012), this can be seen in figure 1.1b.

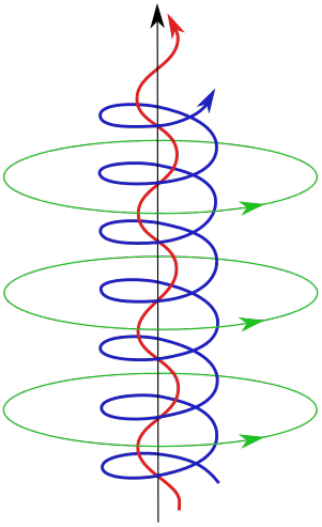

(a) The size of the gyroradius depends on the charge on the particle. The particle denoted by the red arrow has a charge with a magnitude that is greater than that denoted by the blue arrow.(Image obtained at: i.stack.imgur.com/kigHl.png)

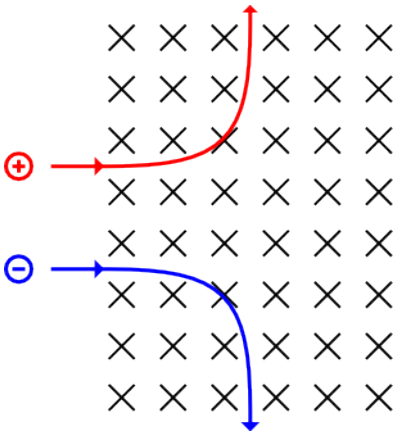

(b) The handedness of the path of the charges particle depends on the sign of the charge on the particle. It can be seen that the positive particle (red) travels in the opposite direction to the negative particle (blue) in the same magnetic field.(Image obtained at: upload.wikimedia.org)

Figure 1.1: The path of particle in a magnetic field and its gyroradius

Unlike the charged particles the neutral particles are free to travel across

field lines although they do not do so completely unimpeded. Although they are not affected by the magnetic field, the neutral particles may interact with the charged particles which are tied to the field lines by colliding with them. These collisions slow down the collapse but the neutral particles will eventually slip past the charged particles and fall toward the centre of gravity of the cloud. The outward diffusion of the charged particles and the magnetic field relative to the neutral particles is known as ambipolar diffusion. The process of ambipolar diffusion is thought to slow down the collapse of molecular clouds as the collisions between the charged and neutral particles results in it taking a greater time for neutral particles to collapse than if they were in free-fall. The collisions also produce heat which cause the thermal energy of the cloud to increase, which will also act to slow down the collapse of the cloud. As the neutral particles move across the field lines they may interact with the charged particles through collisions. The result of the neutral particles colliding with the charged particles is that the thermal energy of the cloud will increase, as heat is produced by these collisions, this process is a result of ambipolar diffusion in the system which will be discussed in more detail in Section 1.2.2. The ambipolar timescale can be derived following the approach taken by Hartmann et al. (2001) as follows;

If it is assumed the gas is weakly ionised, that is, $n_i << n_n$ then the rate of collisions of ions with the neutrals can be given as;

$$R_{col} = n_i < \sigma f(\mathbf{v})\mathbf{v} > \tag{1.44}$$

Where, $\mathbf{v} = v_n - v_i$ is the difference in velocity between the neutrals and the ions. $f(\mathbf{v})$ is the Maxwellian distribution, σ is the collisional cross section.

Next, it is assumed that the ions are frozen to the field, the neutrals are drifting toward the centre of gravity with a velocity v_D and the collisons between neutrals and ions results in the change in momentum of $\mu m_h v_D$,

stopping the drift.

The momentum change is given by;

$$\frac{dP}{dt} = \rho n_i < \sigma f(\mathbf{vv}) > \upsilon_D \tag{1.45}$$

.

The geometry of the system is taken to be cylindrical aligning with the magentic field. So the force due to gravity is given by;

$$-\mathbf{F} = 2\pi RG\rho \tag{1.46}$$

Where, R is the radius of the cylinder. If this gravitational force is then equated to the drag force, then;

$$\rho n_i < \sigma f(\mathbf{vv}) > \upsilon_D = 2\pi RG\rho^2 \tag{1.47}$$

Rearranging this to obtain an expression for the drift velocity, gives;

$$\upsilon_D = \frac{2\pi RG\rho}{n_i < \sigma f(\mathbf{v})\mathbf{v}} > \tag{1.48}$$

We can now give the ambipolar diffusion timescale as $t_{AD} = R/\upsilon_D$, which gives;

$$t_{AD} = \frac{< \sigma f(\mathbf{v})\mathbf{v} >}{2\pi G\mu m_n} \frac{n_i}{n_n} \tag{1.49}$$

Although magnetic fields are thought to slow down the process of gravitational collapse they do not stop it altogether and so eventually the density of the cloud core will become so great that gravitational collapse will overcome the magnetic support of the cloud. This process can take up to 10 Myr. When the gravitational forces overcome the magnetic support, the collapse will accelerate and eventually lead to the birth of a young stellar object (YSO) this can take only 100 kyr (Crutcher, 1999, 2012).

From Cloud Cores to Stars

Protostellar cloud cores are believed to be the direct precursors to stars (Mac Low and Klessen, 2004). The transition of these cores into stars can be divided into four observable phases (Mac Low and Klessen, 2004, Shu et al., 1987).

1. The *Prestellar* Phase : This phase describes the isothermal contraction of the core before a protostar is formed. The gas and dust in the centre of the molecular cloud core undergo gravitational collapse which causes the density of the core to increase. When the density of the core reaches $\approx 10^{10} cm^{-3}$ it becomes optically thick and can no longer radiate energy away freely. As the energy released during the gravitational collapse of the cloud core cannot be efficiently radiated away the temperature of the core rises sharply. This increase in temperature gives rise to a thermal pressure which then acts to prevent the core from collapsing further, although the material outside the core is still undergoing gravitational collapse. When the temperature of the core reaches $\approx 2000K$ molecular hydrogen begins to dissociate, which will absorb energy thereby slowing the increase in temperature. The decreased rate of heating of the core reduces the thermal pressure, thus allowing the core to again become unstable and so the core begins to

collapse again in much the same way as before. The core continues to collapse this time until all of the hydrogen molecules are dissociated which again causes the temperature to rise, and so the thermal pressure increases too, stopping the collapse. The cloud core is now in a state of hydrostatic equilibrium and is now called a protostar (Lada, 1987).

2. The *Class 0* Phase: In this phase the mass of the protostar increases as material continues to be accreted onto the protostar from the surrounding molecular cloud core. The density of the protostar increases due to the infall of material, this makes it more difficult for energy to be radiated away effectively which causes the protostar to enter the class I phase of its evolution. During the Class O phase the mass of the protostellar object is far less than the mass of the surrounding envelope of gas and dust. Any rotation of the original cloud core is also enhanced due to the conservation of angular momentum as the cloud core material falls toward the protostar. Protostars in the class 0 phase have an approximate lifespan of $10^4 yrs$. The bolometric temperatures of these protostars are between 80K and 650K (Lada, 1987, Myers and Ladd, 1993).

3. The *Class I* Phase: In the Class I phase powerful bipolar outflows and an accretion disk develop. Due to the angular momentum of the cloud core the envelope of gas and dust surrounding the protostar will flatten into a disk which rotates around the axis of net rotation of the original cloud. The material of the disk is accreted onto the poles of the protostar along magnetic field lines. Some of the material is ejected from the surface of the protostar and travels in narrow beams from the poles, forming bipolar outflows, these outflows clear away material along the rotational axis of the cloud core, as such the protostar will be visible at optical wave lengths when observed along the outflow direction. Protostars in the class I phase of star formation are identical to classical T-Tauri stars. The lifetime of protostars in this phase is $\approx 10^5 yrs$, with bolometric temperatures of 650K to 1000k (Myers and Ladd, 1993, Lada, 1987).

4. The *Class II* Phase: In this phase most, if not all, of the material from the accretion disk has fallen onto the protostellar object, and so, accretion comes to a stop. In this phase the protostar stops collapsing under its own gravity and settles into equilibrium. The next stages of the protostar's evolution depends on the temperature and density of the core. If the temperature and density are high enough, hydrogen fusion will take place and the protostar will become a main sequence star. If the density and temperature are too low for hydrogen fusion to begin, the protostellar object will become a brown dwarf or other such sub-stellar object. Any material from the accretion disk which was not accreted onto the protostar may at this stage go on to form planetary sysems, comets, asteroids etc. The lifetimes of protostars in the class II phase is $\approx 10^6 yrs$, with bolometric temperatures over 1000K (Myers and Ladd, 1993, Lada, 1987).

1.2 Magnetohydrodynamics

The study of the interaction between magnetic fields and fluids, such as plasmas, is known as Magnetohydrodynamics (MHD). The field of Magnetohydrodynamics is relatively new, with much of its developement being undertaken in the second half of the 20th century, although MHD has been theorized as far back as the early 1800's, with rudimentary experiments being carried out by Michael Faraday. The development of the theory of MHD is due to the advances in computational resources available to run simulations of MHD systems, such as molecular cloud turbulence.

1.2.1 The Magnetohydrodynamic Equations

In order to derive the equations used to model MHD systems one must start with the equations of electodynamics, i.e. Maxwell's Equations, given below (Priest, 2000);

$$\nabla \cdot \mathbf{B} = 0 \tag{1.50}$$

$$\nabla \times \mathbf{B} = \mathbf{j} + \frac{\partial \mathbf{E}}{\partial t} \tag{1.51}$$

$$\nabla \cdot \mathbf{E} = 4\rho_c \tag{1.52}$$

$$\nabla \times \mathbf{E} = -\frac{\partial \mathbf{B}}{\partial t} \tag{1.53}$$

Where $\mathbf{E}$ and $\mathbf{B}$ are the electric and magnetic fields respectively, ρ is the charge density and $\mathbf{j}$ represents the current density. Factors of 4π and the speed of light c have been incorporated into the magnetic and electric field terms.

Before progressing further with the derivation a number of assumptions must be made:

- Local charge neutrality: At large scale the plasma is electrically neutral. That is;

$$\sum_{i=2}^{n} \alpha_i \rho_i \tag{1.54}$$

  where ρ_i is the mass density and α_i is the charge to mass ratio.

- The plasma fluids can be treated as a single fluid: The neutral and ionised fluids are locked together and treated as a single fluid, representing the bulk fluid.

- The plasma is non-relativistic: The flow speed, the Alfvén speed and the sound speed are all much less than the speed of light.

- The Lorentz force is significant relative to other electrostatic forces: The plasma is well coupled to the magnetic field lines.

- The electric current can be described using Ohm's law: Ohm's law for an ideal plasma is given by;

$$\mathbf{J} = \sigma \mathbf{E} \tag{1.55}$$

Using the assumption that the plasma is non-relativistic we can ignore the displacement current in Ampere's law (Equation 1.51) resulting in;

$$\nabla \times \mathbf{B} = \mathbf{j} \tag{1.56}$$

The evolution of the magnetic field can be determined by looking at the Faraday's law (Equation 1.53) and substituting Ohm's law in the rest frame of the plasma;

$$\mathbf{j} \simeq \mathbf{j}' \simeq \sigma \mathbf{E}' \simeq \sigma[\mathbf{E} + (\mathbf{v} \times \mathbf{B})] \tag{1.57}$$

which results in;

$$\frac{\partial \mathbf{B}}{\partial t} = -\nabla \times \left[\frac{\mathbf{j}}{\sigma} - (\mathbf{v} \times \mathbf{b}) \right] \tag{1.58}$$

Then using the fact that $\mathbf{j} = \nabla \times \mathbf{B}$ and the identity $\nabla^2\mathbf{B} = \nabla(\nabla \cdot \mathbf{B}) - \nabla \times (\mathbf{v} \times \mathbf{B})$ one is left with;

$$\frac{\partial \mathbf{B}}{\partial t} = \nabla \times (\mathbf{v} \times \mathbf{B}) - \nabla \times \left(\frac{1}{\sigma}\nabla \times \mathbf{B}\right) = \nabla \times (\mathbf{v} \times \mathbf{B}) + \frac{1}{\sigma}\nabla^2\mathbf{B} \quad (1.59)$$

.

Next the hydrodynamic fluid equations will be modified to take into account the magnetic field, this will give us the remainder of the ideal MHD equations.

The equation for the conservation of momentum is given by;

$$\rho\left(\frac{\partial \mathbf{v}}{\partial t} + \mathbf{v} \cdot \nabla\right) = -\nabla P \quad (1.60)$$

As the Lorentz force is known to effect the motions of particles in a plasma, these effects must be taken into account, The Lorentz force is given by;

$$\mathbf{F} = q(\mathbf{E} + \mathbf{v} \times \mathbf{B}) \quad (1.61)$$

But this can be simplified as the assumption of a quasi-neutral plasma which means the magnetic force is much greater than the electric force, thus the electric field component of the above equation can be ignored giving;

$$\mathbf{F} = q\mathbf{v} \times \mathbf{B} = \mathbf{J} \times \mathbf{B} \tag{1.62}$$

The momentum equation for ideal MHD can then be found by substituting Equation 1.51 into Equation 1.62 and using the result as a source term for Equation 1.60;

$$\mathbf{F} = (\nabla \times \mathbf{B}) \times \mathbf{B} \tag{1.63}$$

$$\rho\left(\frac{\partial \mathbf{v}}{\partial t} + \mathbf{v} \cdot \nabla\right) = -\nabla \mathbf{P} + (\nabla \times \mathbf{B}) \times \mathbf{B} \tag{1.64}$$

The mass conservation equation for a neutral fluid is given by;

$$\frac{\partial \rho}{\partial t} + \nabla \cdot (\rho \mathbf{v}) = \mathbf{0} \tag{1.65}$$

As the mass of a plasma is not affected by magnetic fields, the ideal MHD mass conservation equation is also given by Equation 1.65

Finally, the energy of the system must also be conserved. The energy conservation equation for an ideal fluid is given by;

$$\frac{\partial \rho\epsilon}{\partial t} + \nabla \cdot (\rho\epsilon \mathbf{v}) + (\gamma \rho\epsilon \nabla \cdot \mathbf{v}) = -S \tag{1.66}$$

Where S represents the the energy sources and sinks in the system, ϵ is the internal enegy and γ is the adiabatic index.

1.2.2 A Shift to Multifluid MHD

In the previous section the equations for ideal MHD were derived. In many astrophysical phenomena these equations are insufficient to describe the system accurately, this is due to the fact that many astrophysical systems which can be described using MHD consist of weakly ionised plasmas. Due to the fact that these systems can consist of a neutral fluid and, possibly, a number of charged fluids the assumptions that lead us to the equations of ideal MHD must be relaxed in order to derive a system of equations which detail the physics of all of the fluids in the system in the presence a magnetic field. For example, when modelling a plasma using ideal MHD the plasma is treated as a single fluid. Relaxing the single fluid approximation, that is, treating all of the particle species present in the plasma as seperate fluids opens up the underlying physics of the system being modelled. Each of the fluid species has its own momentum, continuity and energy equations allowing collisions and interactions between the fluids to be modelled. In the multifluid MHD regime Ohm's law must also be generalised, this generalisation takes into account all of the forces acting on the plasma from the different fluid species and accounts for the various effects arising from the interaction of a number of differently charged fluids, such as ambipolar diffusion and the Hall effect. The generalised Ohm's law will be derived in Section 1.2.3.

The presence of multiple fluids in a magnetic field gives rise to a number of interesting physical phenomena, the three most important phenomena for this study are Ohmic Diffusion, Ambipolar Diffusion and The Hall Effect, these phenomena will now be discussed in greater detail.

Ohmic Resistivity: Ohmic Resistivity arises due to collisions between

charged particles which are coupled to the magnetic field lines and other particles, which are travelling at different velocities. These collisions give rise to what can be seen as an electrical resistance, as the charged particles are slowed by their collisions with other particles. In the presence of a magnetic field, the current has two components; one component parallel to the magnetic field and the second component which is perpendicular to the magnetic field. In this work, only the component in the direction parallel to the magnetic field is referred to as ohmic resistivity, the perpendicular component is known as ambipolar resistivity and will be discussed later in this section.

The Hall Effect: As stated previously, the presence of a magnetic field subjects moving, charged particles to the Lorentz force. The Lorentz force causes a deviation of the particle from its original path. In weakly ionised plasmas, for example, the particles which make up the plasma will have differing charges. Dust and ionised particles can be either positively or negatively charged and electrons have a negative charge. As these particles have opposite charges the force acting on them will be in opposite directions, this causes a difference in the velocities of the charged particles which in turn generates an electric field.

Ambipolar Diffusion: The phenomenon of ambipolar diffusion is caused by the collisions between neutral and charged particles. The charged fluid of the plasma is subject to the Lorentz force due to the magnetic field, where as the neutral fluid does not experience the Lorentz force, this creates a difference in velocities between the charged and neutral species. The direction of this velocity difference is perpendicular to the magnetic field. Although the neutral fluid is not subject to the Lorentz force it is coupled to the charged fluid through collisions. These collisions give rise to frictional forces which act to diffuse the magnetic field through the neutral fluid. The magnetic field is diffused in the direction perpendicular to the direction of the magnetic field.

1.2.3 Generalised Ohm's Law

In order to account for the introduction of phenomena such as ambipolar diffusion and the Hall effect a generalised version of Ohm's Law must be employed. In the case of ideal MHD Ohm's law relates the current density of the plasma to the electric field and is given by $\mathbf{J} = \sigma\mathbf{E}$, where σ is the conductivity of the fluid.

If a number of assumptions are made about the system being studied a generalised form of Ohm's Law for weakly ionised plasmas can be derived. The first assumption that is made is that the plasma is weakly ionised, as is generally the case in molecular clouds. This assumption will give rise to a number of other assumptions which will make the derivation of the generalised Ohm's Law more manageable. In a weakly ionised plasma the majority of the particles are neutral so it can be assumed that the velocity of the plasma as a whole can be approximated equal to the velocity of the neutral fluid. So, $\mathbf{v} = \mathbf{v_1}$ where the subscript 1 denotes the neutral species. The assumption is made that the majority of the collisions in the plasma will be with the neutral species and as such collisions between all other species are negligible. It is also assumed that pressure gradients, inertia and the resulting forces of the charged particles are also negligible. This assumption can be made as the mean free path of the neutral species is much greater than the mean free path or gyroradius of the charged species.

The derivation of the weakly ionised generalised Ohm's Law following the approach taken by O'Sullivan and Downes (2006) and Falle (2003) begins with the momentum equation taking into account all of the forces which act on the plasma such as the Lorentz force, pressure gradient and drag forces due to collisions and inertia. It is given by;

$$\alpha_i \rho_i (\mathbf{E} + \mathbf{v_i} \times \mathbf{B}) = \nabla p_i + \rho_i \frac{D_i \mathbf{v_i}}{Dt} - \sum_{j \neq i}^{N} \mathbf{f_{ij}} \tag{1.67}$$

where α_i is the charge to mass ratio of fluid i, ρ_i is the mass density, $\mathbf{v_i}$ is the velocity, p_i is the partial pressure and $\mathbf{f_{ij}}$ is the collisional term between fluids i and j. The importance of the terms in the equation depends entirely on the assumptions being made about the physical system.

The Lagrangian derivative is;

$$\frac{D_i}{Dt} \equiv \frac{\partial}{\partial t} + (\mathbf{v_i} \cdot \nabla) \tag{1.68}$$

With the assumptions made above the momentum equations for the charged particle species reduce to;

$$\alpha_i \rho_i (\mathbf{E} + \mathbf{v_i} \times \mathbf{B}) + \mathbf{f_{i1}} = \mathbf{0} \tag{1.69}$$

for charged fluids $i = 2, ..., N$. The terms ∇p_i and $\rho_i \frac{D_i \mathbf{v_i}}{Dt}$ vanish due to the assumption that pressure gradients and accelerating forces of the charged species are negligible.

The collisional term, $\mathbf{f_{i1}}$ can also be written in terms of transfer of momentum between the charged fluids so the momentum equation can then be written as;

$$\alpha_i \rho_i (\mathbf{E} + \mathbf{v_i} \times \mathbf{B}) + \rho_i \rho_1 K_{i1} (\mathbf{v_1} - \mathbf{v_i}) = 0 \tag{1.70}$$

where K_{i1}, the collisional coefficient relates the collisonal frequency between the neutral fluid and the charge fluid i.

Next, the current density is written as;

$$\mathbf{J} = \sum_{i=2}^{n} \alpha_i \rho_i \mathbf{v_i} \tag{1.71}$$

The momentum equation can be written in the frame of the bulk fluid, by giving the velocities relative to the bulk fluid velocities, $\mathbf{v'_i} = \mathbf{v_i} - \mathbf{v}$, as;

$$\alpha_i \rho_i (\mathbf{E'} + \mathbf{v'_i} \times \mathbf{B}) + \rho_\mathbf{i} \rho_\mathbf{1} \mathbf{K_{i1}} (-\mathbf{v'_i}) = \mathbf{0} \tag{1.72}$$

Note that the electric field is also re-written as that of the equivalent electric field in the reference frame of the bulk mass, $\mathbf{E'} \equiv \mathbf{E} + \mathbf{v} \times \mathbf{B}$.

The Hall parameter, which describes how closely a charged particle is tied to a magnetic field line, is now introduced. The Hall parameter is the ratio of the collisional length- scale and the gyroradius of the species i and is given by;

$$\beta_i = \frac{\alpha_i B}{\rho_1 K_{i1}} \tag{1.73}$$

The momentum equation can now be written in terms of the Hall parameter and the magnetic flux;

$$\alpha_i \rho_i (\mathbf{E'} + \mathbf{v'_i} \times \mathbf{B}) - \frac{\mathbf{B}}{\beta_i} (\alpha_i \rho_i \mathbf{v'_i}) = 0 \tag{1.74}$$

Where ($'$) denotes the reference frame of the bulk fluid.

It is possible to obtain the momentum of the charged species in the x,y and z directions by assuming that the magnetic field is oriented along the z-direction and that the electric field in the x-direction is zero. The momentum for the charged particles in x,y and z directions respectively is given by following set of equations;

$$\alpha_i \rho_i (\upsilon'_{i,y} B) - \frac{B}{\beta_i} \alpha_i \rho_i \upsilon'_{i,x} = 0 \tag{1.75}$$

$$\alpha_i \rho_i (E'_y - \upsilon'_{i,x} B_z) - \frac{B}{\beta i} \alpha_i \rho_i \upsilon'_{i,y} = 0 \tag{1.76}$$

$$\alpha_i \rho_i E'_z - \frac{B}{\beta_i} \alpha_i \rho_i \upsilon'_{i,z} = 0 \tag{1.77}$$

where E'_z and E'_y represent the electric fields in the direction parallel and perpendicular to the magnetic field respectively. $E' \times \mathbf{b}$ defines the electric field in the y-direction where $\mathbf{b}$ is the unit vector in the direction of the magnetic field.

The set of equations above can be rearranged so that the derivation of components of the current density is more straightforward. The simplified momentum equations are as follows;

$$\alpha_i \rho_i \upsilon'_{i,x} = \frac{1}{B} \frac{\alpha_i \rho_i \beta_i^2}{(1 + \beta_i^2)} E'_y \tag{1.78}$$

$$\alpha_i \rho_i v'_{i,y} = \frac{1}{B} \frac{\alpha_i \rho_i \beta_i}{(1+\beta_i^2)} E'_y \tag{1.79}$$

$$\alpha_i \rho_i v'_{i,z} = \frac{1}{B} \alpha_i \rho_i \beta_i E'_z \tag{1.80}$$

In order to obtain the x,y and z components for the current density the simplified momentum equations are summed over the charged particles, which gives;

$$J_x = \sum_{i=2}^{n} \alpha_i \rho_i v'_{i,x} = \frac{1}{B} \sum_{i=2}^{n} \frac{\alpha_i \rho_i \beta_i^2}{1+\beta_i^2} E'_y = \sigma_H E'_y \tag{1.81}$$

$$J_y = \sum_{i=2}^{n} \alpha_i \rho_i v'_{i,y} = \frac{1}{B} \sum_{i=2}^{n} \frac{\alpha_i \rho_i \beta_i^2}{1+\beta_i^2} E'_y = \sigma_\perp E'_y \tag{1.82}$$

$$J_z = \sum_{i=2}^{n} \alpha_i \rho_i v'_{i,z} = \frac{1}{B} \sum_{i=2}^{n} \alpha_i \rho_i \beta_i E'_z = \sigma_\parallel E'_z \tag{1.83}$$

where σ_H is the Hall conductivity, $\sigma_\perp$ is the Pedersen conductivity and $\sigma_\parallel$ is the parallel conductivity which are defined as;

$$\sigma_H = \frac{1}{B}\sum_{i=2}^{n}\frac{\alpha_i\rho_i\beta_i^2}{1+\beta_i^2} \tag{1.84}$$

$$\sigma_\perp = \frac{1}{B}\sum_{i=2}^{n}\frac{\alpha_i\rho_i\beta_i}{1+\beta_i^2} \tag{1.85}$$

$$\sigma_\parallel = \frac{1}{B}\sum_{i=2}^{n}\alpha_i\rho_i\beta_i \tag{1.86}$$

The current density in the frame of the bulk fluid as;

$$\mathbf{J} = \sigma_\parallel \mathbf{E'}_\mathbf{z} + \sigma_\perp \mathbf{E'}_\mathbf{y} + \sigma_\mathbf{H}(\mathbf{E'}_\mathbf{y} \times \mathbf{b}) \tag{1.87}$$

which is in the form $\mathbf{J} = \boldsymbol{\sigma} \cdot \mathbf{E}'$.

The next step in the derivation of the generalised Ohm's Law is to define the conductivity tensor;

$$\sigma = \begin{bmatrix} \sigma_\perp & \sigma_H & 0 \\ -\sigma_H & \sigma_\perp & 0 \\ 0 & 0 & \sigma_\parallel \end{bmatrix} \tag{1.88}$$

The inverse of which is given by;

$$\sigma^{-1} = \begin{bmatrix} \frac{\sigma_\perp}{\sigma_\perp^2+\sigma_H^2} & \frac{-\sigma_H}{\sigma_\perp^2+\sigma_H^2} & 0 \\ \frac{\sigma_H}{\sigma_\perp^2+\sigma_H^2} & \frac{\sigma_\perp}{\sigma_\perp^2+\sigma_H^2} & 0 \\ 0 & 0 & \frac{1}{\sigma_\parallel} \end{bmatrix} = \begin{bmatrix} r_\perp & -r_H & 0 \\ r_H & r_\perp & 0 \\ 0 & 0 & r_\parallel \end{bmatrix} \tag{1.89}$$

where $r_\perp$ is the ambipolar resistivity, $r_\parallel$ is the Ohmic resistivity and r_H is the Hall resistivity.

It is now possible to write the electric field in terms of the current density, i.e. in the form $\mathbf{E}' = \boldsymbol{\sigma}^{-1} \cdot \mathbf{J}$. The electric field is given by;

$$\mathbf{E}' = r_H \mathbf{j}_\perp \times \mathbf{b} + r_\parallel \mathbf{J}_\parallel - r_\perp \mathbf{J}_\perp \tag{1.90}$$

where $\mathbf{J}_\perp$ is the current density perpendicular to the magnetic field and $\mathbf{J}_\parallel$ is the current density parallel to the magnetic field, this can also be written as;

$$\mathbf{E}' = r_H \frac{(\mathbf{J} \times \mathbf{B})}{B} + r_\parallel \frac{(\mathbf{J} \cdot \mathbf{B})\mathbf{B}}{B^2} - r_\perp \frac{(\mathbf{J} \times \mathbf{B}) \times \mathbf{B}}{B^2} \tag{1.91}$$

Thus, in the rest frame the generalised Ohm's law for a weakly ionised plasma can be written as (Ciolek and Roberge, 2002, Falle, 2003);

$$\mathbf{E} = -\mathbf{v} \times \mathbf{B} + r_H \frac{(\mathbf{J} \times \mathbf{B})}{B} + r_\parallel \frac{(\mathbf{j} \cdot \mathbf{B})\mathbf{B}}{B^2} - r_\perp \frac{(\mathbf{J} \times \mathbf{B}) \times \mathbf{B}}{B^2} \tag{1.92}$$

thereby ending our derivation of the generalised Ohm's Law for a weakly ionised plasma.

Chapter 2

Turbulence in Molecular Clouds

As stated in Section 1.1.2, molecular clouds are thought to be turbulent systems. It is believed that the presence of these turbulent motions have a substantial impact on the evolution of molecular clouds (Downes, 2012, Momferratos et al., 2014, Zhdankin et al., 2014, Servidio et al., 2010). In order to discuss the process of turbulence in multifluid MHD systems, like those found in molecular clouds we outline what turbulence is in the regime of hydrodynamics before extending our discussion to include these systems.

2.1 Hydrodynamic Turbulence

Turbulence is an extremely common physical phenomenon, occurring in daily life whenever almost all fluids are in motion. Examples of common turbulent flows are those around a car or the smoke rising from a lit cigarette, although the first few centimetres of smoke is laminar the flow becomes turbulent as the flow velocity and Reynolds number increase. Although turbulence is so common there exists no physical definition of it, there is instead a set of characteristics which can be used to determine if a flow is turbulent (Davidson, 2011), these features are as follows;

- *Irregularity*: The motion of a turbulent fluid is chaotic and extremely irregular, but is deterministic and is described using the Navier-Stokes equation. The length-scale of turbulent motions (eddies) varies considerably, ranging from system size, to small eddies which dissipate energy through viscous forces.

- *Diffusivity*: Turbulent motions act to increase diffusivity in a system. Momentum exchange and heat transfer increase due to turbulent flow.

- *Dissipation*: Energy is dissipated by turbulent motions. Energy is injected into a system at large scales, a cascade process then acts to transfer energy from larger eddies to smaller eddies, which in turn transfer energy to even smaller eddies and so on until a dissipation length-scale is reached and the energy is dissipated in the form of heat.

- *3-Dimensional*: The values of the properties which describe a turbulent flow fluctuate rapidly in 3-Dimensions. Although we can treat the flow as 2-dimensional, i.e. the system geometry is 2-D such as flows in a soap film, if the governing equations are time-averaged.

- *Reynolds Number*: In order for turbulence to occur the Reynolds number of flow is generally rather high. Reynolds number is defined by

$$R = \frac{UL}{\nu} \tag{2.1}$$

Where, U is the characteristic velocity of the flow, L is the characteristic length-scale and ν is the kinematic viscosity which is defined as; $\nu \equiv \frac{\mu}{\rho}$

- *Continuous*: Due to the fact that the length-scales of turbulent motions are very much greater than molecular length-scales the flow can be treated as a continuum.

2.1.1 Turbulent Scales

As mentioned in the previous section, the length-scales associated with turbulent flows span the continuum. Energy is injected into the system at rather large scales, for example it is believed that a driving mechanism for molecular cloud turbulence is shock waves from supernovae. The energy injected into the system by these shock waves is dissipated at small length-scales by viscous forces. The process by which energy is transferred from the length-scales at which is it injected into the system to the small scales at which it is dissipated is known as the turbulent energy cascade. During the turbulent energy cascade the large scale turbulent motions interact with smaller scale motions and kinetic energy is transferred from large scales to smaller scales, this interaction is then repeated for smaller and smaller scales until the length-scales are small enough for viscous forces to be to non-negligible and the energy is dissipated as heat. If the turbulence is in a statistical steady state the rate at which energy is transferred is independent of the size of the eddy, that is; the energy transferred from a large eddy to a slightly smaller eddy is the same for each size. A diagram of the turbulent energy cascade is given in figure 2.1. The vast majority, $\approx 90\%$, of energy in a system is dissipated at the smallest scales, known as the Kolmogorov Scales (Davidson, 2011).

2.1.2 The Kolmogorov Energy Spectrum

The process of turbulent cascade outlined in the previous section, by which energy is transferred from large scale eddies to smaller and smaller eddies until dissipation was used by Kolmogorov (1941) laying the foundations of the current theory of turbulent scaling. Kolmogorov assumed that the tur-

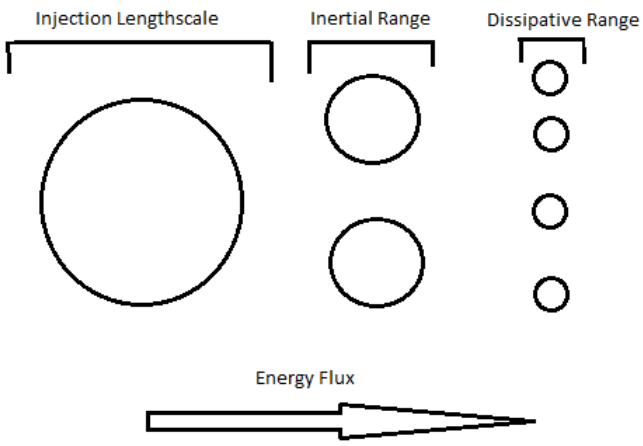

Figure 2.1: Diagram of the turbulent energy cascade showing that energy is transferred from large scales to smaller scales

bulence itself is the origin of viscosity in the flow and as such the energy spectrum should be independent of viscosity.

In order to obtain the Kolmogorov Spectrum for an incompressible fluid the energy dissipation rate, or energy transfer rate is defined as (Padmanabhan, 2000);

$$\dot{E} \simeq (\frac{1}{2}u^2)(\frac{u}{l}) \simeq \frac{u^3}{l} \tag{2.2}$$

where $\dot{E}$ is the energy transfer rate, u is the velocity of the eddy and l is the length-scale of a generic eddy. The first term in the above equation gives the amount of energy contained in an eddy of length l, the second term gives the inverse of the time it takes for energy to be transferred at this length-scale.

The viscosity for the turbulent flow is then given by;

$$\nu \approx ul \approx \dot{E}^{1/3} l^{4/3} \tag{2.3}$$

In steady state, energy cannot accumulate in eddies of a certain length-scale in the inertial range and so this energy much be transferred to smaller and smaller scales at a constant rate until it is dissipated. The energy distribution of the cascade at the injection length-scale ,L , is only determined by the driving mechanism. At the bottom of the cascade, at the dissipation length-scale, the energy distribution is determined only by viscous forces (Mac Low and Klessen, 2004). Between the dissipative scale and the driving scale is a region known as the inertial range. In the inertial range kinetic energy can transfer from large eddies to smaller eddies without the influence of driving or viscous forces. Figure 2.2 shows the schematic energy spectra for the turbulent energy cascade. The three distinct regions of the energy spectrum discussed previously are shown.

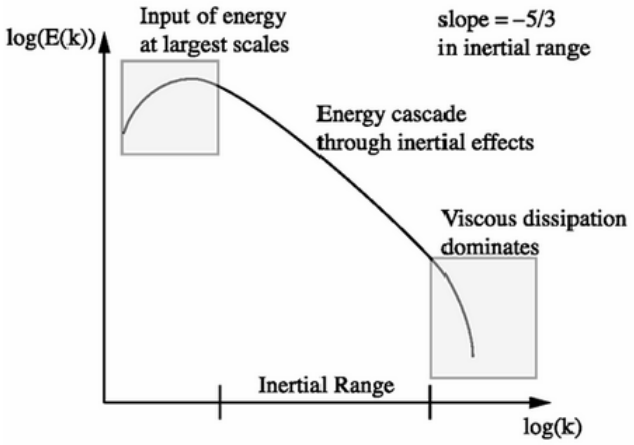

Figure 2.2: Schematic energy spectrum for turbulent cascade. It can be seen that in the dissipative range the energy distribution drops of steeply, where as more energy is found at the driving length-scale. (image from:Berselli (2005))

The smallest length-scale, or the Kolmogorov length-scale, is given by;

$$l_K = \left(\frac{\nu^3}{\dot{E}}\right)^{1/4} \tag{2.4}$$

The characteristic time-scale of the energy dissipation is then;

$$t_K = \left(\frac{\nu}{\dot{E}}\right)^{1/2} \tag{2.5}$$

Using equations 2.5 and 2.4 the characteristic velocity of eddies at the Kolmogorov scale is;

$$\upsilon_K = (\nu\dot{E})^{1/4} \tag{2.6}$$

Next, we employ the Navier-Stokes equation;

$$\frac{du_i}{dt} = \nu\frac{\partial^2 u_i}{\partial x_i \partial x_j} \tag{2.7}$$

So that the energy transfer rate per unit volume can be obtained by taking the scalar product with u_i and integrating over the volume as follows;

$$\dot{E} = \int dV \frac{1}{2}\frac{du^2}{dt} = \nu \int dV u_i \nabla^2 u_i = \nu \int dS n_j u_i \frac{\partial u_i}{\partial x_j} - \nu \int dV \left(\frac{\partial u_i}{\partial x_j}\right) \tag{2.8}$$

On the right-hand-side of equation 2.8, the surface integral vanishes and the integral over the volume is always positive, therefore the fluctuations in the fluid are always dissipative due to viscous coupling (Shore, 2003). By defining $E(k)$ to be a spectrum which is a function of the wavenumber k, then the energy transfer rate can be written as;

$$\dot{E} = -\nu \int E(k) k^2 dk \tag{2.9}$$

If equation 2.3 is substituted for ν in equation 2.9 and both sides of the resulting equation are integrated then;

$$\dot{E}^{2/3} k^{4/3} = \int E(k) k^2 dk \tag{2.10}$$

so,

$$E(k) = \frac{1}{k^2} \dot{E}^{2/3} \frac{dk^{4/3}}{dk} \approx \dot{E}^{2/3} k^{-5/3} \tag{2.11}$$

This is known as the Kolmogorov power spectrum for velocity fluctuations. If it is assumed that the system is in steady state then the velocity fluctuations are just the inverse of the density fluctuations so the spectrum will remain the same for density fluctuations. This fact leads to the assumption that the process of the energy cascade does not depend on the viscosity of the fluid. The physical meaning of the Kolmogorov spectrum is that there is some small length-scale at which energy dissipation will dominate the spectrum, but at length-scales larger than this a steady state has been reached in which eddies which transfer their energy to smaller scales are replaced

by eddies of the same vorticity and size by the breaking up of larger eddies (Shore, 2003). This allows for the rate of energy transfer to the smallest scales to remain constant.

2.1.3 MHD Turbulence

MHD turbulence is believed to be an important process for astrophysical processes such as star formation, cosmic ray propagation and stellar winds (Brandenburg and Lazarian, 2013).
The theory of MHD Turbulence is quite similar to that of the hydrodynamic turbulence discussed in the previous section. In MHD turbulence, the energy which is injected into the system at large scales undergoes a cascade to smaller and smaller scales until it is dissipated, as is the case with hydrodynamic turbulence. However, MHD turbulence differs from hydrodynamic turbulence because instead of fluctuations only in the fluid properties, i.e. its velocity, there exists also fluctuations in the magnetic field. A further difference between the two is that unlike hydrodynamic turbulence, which at small scales becomes isotropic, the MHD turbulent cascade becomes more anisotropic at small scales. The MHD cascade becoming more anisotropic results from the fact that there exists no scale at which the fluid is not affected by the magnetic field (Tobias et al., 2011).

In order to extend this to the MHD case a plasma threaded by a uniform magnetic field ($\mathbf{B}_0$) must be considered. The magnetic field is subject to small wave-like perturbations along the magnetic field. This turbulence is anisotropic and known as Alfvénic turbulence (Tobias et al., 2011).

Weak Turbulence

A model of weak MHD turbulence was developed by Iroshnikov (1963) and independently by Kraichnan and Nagarajan (1967). The Iroshnikov-Kraichnan (IK) model proposes that Alfvén waves propagating along a strong magnetic

field have weak interactions.

Two wave packets of size $l_\perp$ perpendicular to the field line are considered. These wave packets travel in opposite directions along the field line at a velocity of, υ_A, the Alfvén velocity. In the IK model it is assumed that the wave packets are isotropic so their size parallel to the field line is equal to their size perpendicular to the field, $l_\parallel = l_\perp = \lambda$. It is also assumed that interactions mainly occur between eddies of comparable size, it is then possible to find the distortion of each wave packet during a collision, i.e. one crossing time λ/υ_A. In order to find these distortions we first write the MHD equations in terms of the Elsasser variables, $\mathbf{z} = \mathbf{v} \pm \mathbf{b}$, as follows (Tobias et al., 2011);

$$\left(\frac{\partial}{\partial t} \mp \mathbf{v}_A \cdot \nabla\right)\mathbf{z}^\pm + (\mathbf{z}^\mp \cdot \nabla)\mathbf{z}^\pm = -\nabla P + \frac{1}{2}(\nu+\eta)\nabla^2\mathbf{z}^\pm + \frac{1}{2}(\nu-\eta)\nabla^2\mathbf{z}^\mp + \mathbf{f}^\pm \tag{2.12}$$

Where, $\mathbf{v}$ is the fluctuating velocity of the plasma, b is the magnetic field fluctuations which is normalised by; $\sqrt{4\pi\rho_0}$. In equation 2.12 P is the pressure, which includes the plasma pressure and magnetic pressure, $P = (p/\rho_0 + b^2/2)$ and $\mathbf{f}^{pm}$ are forces such as driving forces,etc. $\mathbf{v}_A = \mathbf{B}_0/\sqrt{4\pi\rho_0}$, is the uniform field contribution.
For an incompressible fluid the pressure term in equation 2.12 is not an independent function, it ensures the incompressibility of the Elsasser fields, $\mathbf{z}^+$ and $\mathbf{z}^-$.

If driving forces and dissipation are neglected, an exact nonlinear solution of the MHD equations exists, representing an Alfvénic wave packet propagating along a field line in the direction of, $\mp\mathbf{v}_A$, that is, $\mathbf{z}^\pm(\mathbf{x}, t) = F^\pm(\mathbf{x} \pm \mathbf{v}_A t)$, where $F^\pm$ is some arbitrary function. So, a wave packet ($\mathbf{z}^\pm$) will only be distorted when it reaches a region where $\mathbf{z}^\mp$ is non-zero otherwise the wave

packet will propagate along the field line undistorted. Therefore, the nonlinear interactions are only due to wave packets propagating in opposite directions.

The Elsasser energies, given by;

$$E^+ = \int (\mathbf{z}^+)^2 d^3x \tag{2.13}$$

and

$$E^- = \int (\mathbf{z}^-)^2 d^3x \tag{2.14}$$

are conserved and undergo a cascade to small scale due to the wave packet interactions described previously.

The picture of MHD turbulence at this point of the derivation is of Alfvén wave packets which interact nonlinearly. This interaction causes the wave packets to distort and break into smaller and smaller wave packets until their energy is dissipated, much like the energy cascade in hydrodynamic turbulence.

By comparing the linear terms, $(\mathbf{v}_A \cdot \nabla)\mathbf{z}^\pm$, describing the advection of wave packets along the field line and the nonlinear terms, $(\mathbf{z}^\mp \cdot \nabla)\mathbf{z}^\pm$, describing the distortion of the interacting wave packets and the redistribution of energy to smaller length-scales it is possible to find the strength of the interaction between wave packets. If b_λ is the RMS of the fluctuations of the magnetic field in the direction perpendicular to the directions of the magnetic field at length-scale $\lambda \propto 1/k_\perp$ and the wavenumber of these fluctuations in the direction parallel to the magnetic field is assumed to be $k_\parallel$. The magnetic and velocity fluctuations for Alfvén waves are of the same order. Therefore,

$(\mathbf{v}_A \cdot \nabla)\mathbf{z}^{\pm} \sim v_A k_{\parallel} b_{\lambda}$ and $(\mathbf{z}^{\mp} \cdot \nabla)\mathbf{z}^{\pm} \sim k_{\perp} b_{\lambda}^2$. If the linear term dominates, such that;

$$k_{\parallel} v_A \gg k_{\perp} b_{\lambda} \tag{2.15}$$

then the turbulence is said to be weak. The distortion of each wave packet is given by;

$$\delta v_{\lambda} \approx \left(\frac{v_{\lambda}^2}{\lambda}\right)\left(\frac{\lambda}{v_A}\right) \tag{2.16}$$

After N collisions with uncorrelated, counter-propagating waves the distortions add up to become significant. The number of collisions, N, is given by;

$$N \approx \left(\frac{v_{\lambda}}{\delta v_{\lambda}}\right)^2 \approx \left(\frac{v_A}{v_{\lambda}}\right)^2 \tag{2.17}$$

Due to the fact that the wave packet interactions are weak, a wave packet must undergo many collisions before its energy is transferred. The time it takes for a wave to transfer its energy to smaller scales is given by;

$$\tau_{IK}(\lambda) \approx N\left(\frac{\lambda}{v_A}\right) \approx \lambda\left(\frac{v_A}{v_{\lambda}^2}\right) = \frac{\lambda}{v_{\lambda}}\left(\frac{v_A}{v_{\lambda}}\right) \tag{2.18}$$

As with hydrodynamic turbulence the energy flux is required to be con-

stant, that is;

$$\dot{E} = \frac{v_\lambda^2}{\tau_{IK}(\lambda)} = const \tag{2.19}$$

So, then the fluctuating fields scale as $v_A \propto b_\lambda \propto \lambda^{1/4}$, resulting in the energy spectrum;

$$E_{IK}(k) \approx |v_k|^2 4\pi k^2 \propto k^{-3/2} \tag{2.20}$$

This comes from the fact that the spectrum of the velocity field scales as $k^{-7/2}$. The spectrum of the velocity field is the Fourier transform of the second order structure function of the velocity field, which scales as $\lambda^{1/2}$ (Tobias et al., 2011).

Up until this point the turbulence has been assumed to be isotropic, by dropping this assumption the theory can be extended to be anisotropic which, as mentioned previously, is the reality for MHD turbulence.

It is possible to assume that weak turbulence consists of weakly interacting pseudo-Alfvénic and shear-Alfvénic waves. letting k_1 and k_2 be the wave vectors of two Alfvén waves then according to Shebalin et al. (1983) these waves can interact with another wave only if the resonance conditions;

$$\mathbf{k}_1 + \mathbf{k}_2 = \mathbf{k} \tag{2.21}$$

and

$$\omega^{+}(k_1) + \omega^{-}(k_2) = \omega(k) \tag{2.22}$$

are satisfied, where, $\omega(k)$ is the frequency of the Alfvén waves. The component of the wave vectors parallel to the magnetic field, $k_{1\parallel}$ and $k_{2\parallel}$ will have opposite signs because, as mentioned previously, only waves travelling in opposite directions along the field will interact. In the case of either $k_{1\parallel}$ or $k_{2\parallel}$ then the solution to the resonance equations only exists if $\omega(k_2) = 0$ or $\omega(k_1) = 0$ so that $k_{1\parallel}$ or $k_{2\parallel}$ is zero. So the $k_\parallel$ component of the resulting wave vector remains unchanged but the $k_\perp$ component can be larger than the other two waves. So, energy can cascade in the direction perpendicular to the field but parallel cascade is prevented (Shebalin et al., 1983).

From equation 2.12, and if the polarization of pseudo-Alfvén waves is essentially parallel to the field when $k_\perp \gg k_\parallel$ then;

$$(\mathbf{z}_p^{\pm} \cdot \nabla)\mathbf{z}_s^{\mp} \sim z_p^{\pm} k_\parallel z_s^{\mp} \tag{2.23}$$

This equation describes the influence the pseudo-Alfvénic modes ($\mathbf{z}_p$) have on the shear-Alfvénic modes and;

$$(\mathbf{z}_s^{\pm} \cdot \nabla)\mathbf{z}_s^{\mp} \sim z_s^{\pm} k_\perp z_s^{\mp} \tag{2.24}$$

describes the interaction of shear-Alfvén modes ($\mathbf{z}_s$) with each other. It then follows that the shear-Alfvénic modes are not coupled to the pseudo-Alfvénic modes(Goldreich and Sridhar, 1995), because of the fact that the

energy cascade is prevented in the direction parallel to the field, $k_{\|} = 0$. Therefore, pseudo-Alfvén modes are advected by shear-Alfvén modes passively. Thus, the two modes will have the same spectra, because the spectrum of a passively advected scalar is the same as the spectrum of the velocity field which advects it (Tobias et al., 2011). This spectrum can be obtained in a similar fashion to the IK spectrum, discussed previously in this section.

The length-scale of an interacting wave packet in the direction perpendicular to the field is, λ, its length-scale in the parallel direction is then given as, l. Unlike the IK case detailed previously, the length-scale of the wave packet in the direction parallel to the field is unchanged. The crossing time is then given by (l/υ_A). The distortion of a wave packet during a single interaction is then given by;

$$\delta\upsilon_\lambda \sim \left(\frac{\upsilon_\lambda^2}{\lambda}\right)\left(\frac{l}{\upsilon_A}\right) \tag{2.25}$$

The number of interactions a wave packet must undergo before its energy is transferred to smaller scales is;

$$N \approx \left(\frac{\upsilon_\lambda}{\delta\upsilon_\lambda}\right)^2 \approx \frac{\lambda^2\upsilon_A^2}{l^2\upsilon_\lambda^2} \tag{2.26}$$

The time it takes for the energy to be transferred is;

$$\tau_\omega \approx N\left(\frac{l}{\upsilon_A}\right) \tag{2.27}$$

As the energy flux, again, has to be constant $\dot{E} \approx v_\lambda^2/\tau = const$, the energy spectrum can then be found to be;

$$E(k_\perp) \propto k_\perp^{-2} \tag{2.28}$$

But, as $k_\perp$ becomes large then the turbulence should become strong and equation 2.15 is no longer satisfied. The case of strong turbulence is outlined in the following section.

Goldreich-Sridhar Turbulence

In the case of strong turbulence the magnetic field lines are bent considerably by fluctuations in the velocity field and as such a single wave packet interaction can impart a significant distortion. The strong deviation of the magnetic field means that small wave packets would not be guided by the mean field but by a local field which is stirred up by larger wave packets(Tobias et al., 2011).

As stated in the previous section when $k_\perp$ is large the turbulence becomes strong so the condition 2.15 is broken. A conjecture put forward by Goldreich and Sridhar (1995) proposes that the linear and nonlinear terms should be balanced;

$$k_\parallel v_A \approx k_\perp b_\lambda \tag{2.29}$$

This new condition is called "critical balance". Due to critical balance the time-scale for the distortion of a wave packet is;

$$\tau_N = \frac{\lambda}{\upsilon_\lambda} \tag{2.30}$$

So, as the Alfvén velocity of the wave packet is finite the distortion cannot travel along the field line more than a distance of;

$$l \approx \upsilon_A \tau_N \tag{2.31}$$

Another consequence of critical balance is that the displacement of a magnetic field line in the direction perpendicular to the field by a wave packet of length l is;

$$\xi \approx \frac{b_\lambda l}{\upsilon_A} \tag{2.32}$$

In the regime of strong turbulence this is equal to λ, which is the wave packet size in the direction perpendicular to the field (Tobias et al., 2011).

Using 2.30 and the constant energy flux condition, the energy spectrum for strong turbulence is;

$$E_{GS}(k_\perp) \propto k_\perp^{-5/3} \tag{2.33}$$

which as seen in section 2.1.2 is the form of the Kolmogorov spectrum.
Strong turbulence becomes more and more anisotropic at small scales. As

wave packets get smaller they become more elongated along the field due to the critical balance condition and the scaling $l \propto \lambda^{2/3}$ (Tobias et al., 2011).

2.2 Energy Dissipation in MHD Turbulence

As mentioned previously, energy in a turbulent system is transferred from large scales to smaller and smaller scales until it is dissipated, in hydrodynamic turbulence this happens due to viscous forces at small length-scales. In MHD turbulence the magnetic field can be a mechanism through which energy is dissipated, such dissipation of energy gives rise to magnetic heating(Priest, 2000).

2.2.1 Magnetic Heating

As discussed in section 2.1, the turbulent motions of a plasma act to stir up magnetic field lines. The motion of these field lines can produce a number of different types of wave, including magnetoacoustic waves and Alfvén waves. A wave propagating in the direction perpendicular to the direction of the magnetic field, caused by the compression of the plasma and driven by magnetic and plasma pressures is called a magnetoacoustic wave (Soler et al., 2013). Magnetoacoustic waves propagate until they steepen sufficiently and form a shock structure. The process by which shocks form and dissipate energy will be discussed later in this section. Alfvén waves in comparison require nonlinear interactions to dissipate their energy through magnetoacoustic waves. The dissipation of energy through Alfvén wave propagation takes place when the linear treatment of wave propagation through uniform media no longer is applicable as is the case in the following situations (Priest, 2000);

- When the perturbation is large enough that nonlinear effects become important.

- The velocity of the perturbation is small enough that the wavelength of the perturbation is greater than the scale height of the system.

- The magnetic field lines move more slowly than the Alfvén waves, such that;

$$\tau > \tau_A = \frac{L}{\nu_A} \tag{2.34}$$

where, τ is the time it takes for the magnetic field lines to travel the length-scale of the system (L), τ_A is the Alfvén travel time, and ν_A is the Alfvén velocity.

This case is applicable to models where the ends of the magnetic field lines are anchored at each end to a surface and these ends are free to travel across the surface. The solar corona is an example of such a system.
The condition can be written more generally as;

$$\lambda > L \tag{2.35}$$

That is, the wavelength of the Alfvén wave exceeds the length-scale of the system.

It is the final condition above which allows for the dissipation of energy through current sheets.

2.2.2 Current Sheets

The production of current sheets may occur in a number of ways. The turbulent motion of the molecular cloud may act to cause changes in the morphology of the magnetic field which permeates the cloud. The morphological changes to the magnetic field result in the separation of the magnetic field lines in some regions and the pushing together of field lines in others. It is at the interface between the magnetic field lines which are being brought into close proximity that current sheets form due to the increase in the energy density of the magnetic field. Plasma flows slowly from the surrounding areas onto the sides of the current sheet. The plasma particles are then accelerated in the current sheet (Siversky and Zharkova, 2009) along the directions parallel to the field lines due to the fact that the field lines are converging. The increased velocity of the plasma in the confined region of the current sheet increases the rate of collisions between particles, these collisions produce heat which is then dissipated, an illustration of this process can be seen in figure 2.3.
Energy is also dissipated from current sheets in the form of shocks which emanate from the ends of the current sheet(Priest, 2000). These shocks form as a result of particles, which were accelerated in the current sheet, interacting with the relatively slow moving plasma outside of the current sheet. The sharp increase in density at the shock front leads to the increase in thermal energy, this energy is then dissipated as heat. The vast majority of dissipation in current sheets is as a result of these shocks, although Ohmic heating is also present.
The breakdown down of magnetostatic equilibrium can also lead to the formation of current sheets according to Vekstein and Priest (1993).

The energy may also be dissipated from the magnetic field through the process of magnetic reconnection. Magnetic reconnection occurs when two oppositely oriented field lines are pushed too close together, this causes the original field lines to break and then reconnect with the oppositely oriented field line, an illustration of this can be seen in figure 2.4.

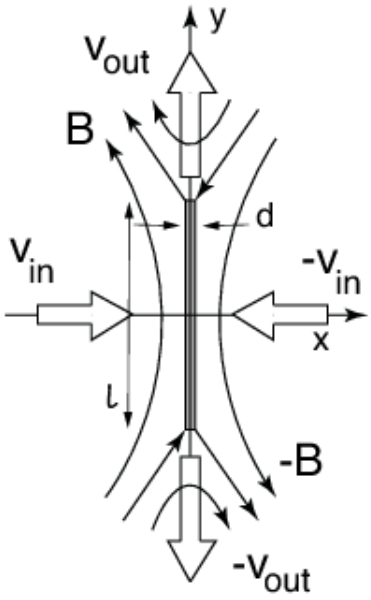

Figure 2.3: Illustration of the formation of a current sheet. Magnetic field lines are pushed close together, plasma flows into the current sheet perpendicular to the magnetic field lines at velocity V_{in}, undergoes a velocity increase and flows out of the current sheet in the direction parallel and anti-parallel to field lines at velocity V_{out}. (Image obtained from: Treumann and Baumjohann (2013))

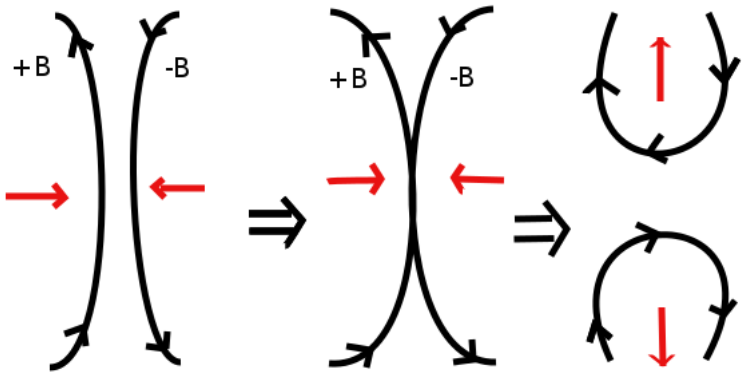

Figure 2.4: Basic principle of magnetic reconnection.

Tucker (1973) and Levine (1974) demonstrated that dissipation through current sheets was sufficient for heating in the solar corona, although this question is still very much open.

The heating mechanisms of the solar corona are the subject of a paper by Zhdankin et al. (2014) in which the intermittency of MHD turbulence is investigated. It is suggested that energy is dissipated in current sheets which span a large range of length-scales, from what Zhdankin et al. (2014) refer to as "coherent structures" to "nano-flares". The definition of each of these terms is given as follows;

- Coherent structures: A coherent structure is a dissipative structure with length-scales which span the inertial range.

- Nano-flares: A nano-flare is a dissipative structure with length-scales comparable with the dissipative range.

By determining the length-scales of the dissipative current sheets, Zhdankin et al. (2014) found that the probability distribution of energy dissipation rates is a power-law with an index of -2.0. Observations of the solar corona have found that during periods when the solar activity is quite low, i.e. no active flaring is occurring, the probability distribution is a power-law of which the index is also -2.0. An index of -2.0 suggests that there is no preferred length-scale at which energy is dissipated from the system. It then follows that the energy is dissipated in a combination of both coherent structures and nano-flares. The lengths and widths of the coherent structures can span the system size as they are dissipative structures, their thickness is well within the dissipative range(Zhdankin et al., 2014). This work was expanded upon by Zhdankin et al. (2015) in which the evolution of the coherent structures over time is investigated. The work in both Zhdankin et al. (2014) and Zhdankin et al. (2015) uses the model of Reduced MHD (RMHD)

turbulence and as such the effects of ambipolar diffusion and the hall effect are not present in the simulations.

The effects of ambipolar diffusion on energy dissipation in MHD turbulence was investigated by Momferratos et al. (2014). This work found, similarly to that of Zhdankin et al. (2014), that dissipation occurs mostly in thin, sheet like structures which have lengths and widths in the inertial range but thicknesses in the dissipative range. The effect of ambipolar diffusion on the system is to steepen the magnetic gradient which allows for thinner dissipative structures while keeping their lengths and widths in the inertial range. This is in line with the work of Brandenburg and Zweibel (1994), where it is proposed that ambipolar diffusion acts to create sharp structures around magnetic null points. Momferratos et al. (2014) found that areas of different types of dissipation, namely; viscous, ambipolar and Ohmic dissipation are well separated in space at low dissipation rates. At high dissipation rates viscous dissipation becomes negligible but Ohmic and ambipolar dissipation are not clearly separated. The geometry of the dissipation regions is such that they occupy only $\approx 3\%$ of the volume but account for $> 30\%$ of the dissipation in the system.

Chapter 3

Numerical Methods

In order to solve the governing equations of magnetohydrodynamics numerical simulations must be employed. This is due to the fact that the systems of equations become far too nonlinear to solve analytically and so numerical methods must be devised to discretize and solve the equations. Once methods of solving the equations of MHD have been found one can then use these to create computational simulations of the physical phenomena one wishes to study. These computational simulations are of great importance to the study of astrophysics as they allow for the modelling and study of various astrophysical objects. Simulations also allow for the detailed study of the evolution of the objects of interest. However, the amount of detail one may obtain from simulations is dependent on the computational resources available to the researcher. In more recent times simulations of MHD have become a lot more detailed due to the huge increases in computer power and the development of codes which implement parallel processing.

This chapter will detail and explain the numerical methods and codes used in this work, as well as outline a number of shock-tube test cases which demonstrate the validity of the code.

3.1 HYDRA Code

The numerical code used in this work to conduct computational simulations of molecular cloud turbulence is the HYDRA code (O'Sullivan and Downes, 2006, 2007). HYDRA uses an explicit scheme to integrate the multifluid MHD equations for weakly ionised plasmas. Due to the fact it uses an explicit scheme HYDRA can run using parallel computing by decomposing the computational domain thereby making it possible to carry out large-scale, high-resolution simulations.

3.1.1 Multifluid MHD Equations

The equations which are solved by HYDRA are as follows;

$$\frac{\partial \rho_i}{\partial t} + \nabla \cdot (\rho_i \mathbf{v}_i) = 0 \tag{3.1}$$

$$\frac{\partial \rho_1 \mathbf{v}_1}{\partial t} + \nabla \cdot (\rho_1 \mathbf{v}_1 \mathbf{v}_1 + p_1 \mathbf{I}) = \mathbf{J} \times \mathbf{B} \tag{3.2}$$

$$\frac{\partial \mathbf{B}}{\partial t} + \nabla \cdot (\mathbf{v}_1 \mathbf{B} - \mathbf{B}\mathbf{v}_1) = -\nabla \times \mathbf{E}' \tag{3.3}$$

$$\alpha_i \rho_i (\mathbf{E} + \mathbf{v} \times \mathbf{B}) + \rho_i \rho_1 K_{i1} (\mathbf{v}_1 - \mathbf{v}_i) = 0 \tag{3.4}$$

$$\nabla \cdot \mathbf{B} = 0 \tag{3.5}$$

$$\mathbf{J} = \nabla \times \mathbf{B} \tag{3.6}$$

$$\sum_{i=2}^{N} \alpha_i \rho_i = 0 \tag{3.7}$$

$$\sum_{i=2}^{N} \alpha_i \rho_i \mathbf{v}_i = \mathbf{j} \tag{3.8}$$

where the subscripts used in the above equations denote the species, the subscript one denotes the neutral species. The variables are defined as follows; ρ_i is the mass density, $\mathbf{v}_i$ is the velocity, and p_i is the pressure of the fluid species i. The collisional coefficient with the neutral fluid is K_{i1}, α_i is the charge to mass ratio. $\mathbf{J}$,$\mathbf{B}$ and $\mathbf{I}$ denote the current density, the magnetic flux density and the identity matrix. The electric field $\mathbf{E}'$ is related to the full electric field by the expression $\mathbf{E}' = \mathbf{E} + \mathbf{v}_1 \times \mathbf{B}$. The equation of state;

$$c_s^2 = \frac{p_1}{\rho_1} \tag{3.9}$$

is used to close the above system of equations under the isothermal approximation. In the above equation of state c_s is the isothermal speed of sound.

The above set of equations can then be solved using HYDRA. The way in which HYDRA solves the multifluid MHD equations will be detailed in the next section.

3.1.2 Solving The Multifluid MHD Equations

The HYDRA code uses an explicit scheme to integrate the multifluid MHD equations outlined in the previous section. The scheme uses finite-volume shock capturing methods which are 2^{nd} order accurate in both time and space.

Numerical Algorithm

In order to solve the above equations it is assumed that the solution of the equations is piecewise constant at time t^n on a uniform mesh. The spacing of the mesh is h in the x,y and z directions and one is seeking the solution at the time $t^{n+1} = t^n + \tau$. If the position of a cell in 3-D space is given by (i, j, k) then the state in any given cell represents the volume average over $(i-\frac{1}{2})h \leq x \leq (i+\frac{1}{2})h$, $(j-\frac{1}{2})h \leq y \leq (j+\frac{1}{2})h$ and $(k-\frac{1}{2})h \leq z \leq (k+\frac{1}{2})h$.

In order to obtain a full solution at t^{n+1} finite volume methods are employed for equations 3.1 - 3.3. The time integration of the equations is split into a number of operations which are carried out to 2^{nd} order accuracy in both space and time. 2^{nd} order accuracy is maintained by permuting the order of operations over successive time steps. The operations necessary for the integration are as follows;

1. The neutral fluid of the plasma is advanced. The continuity equation, equation 3.1, is used to advance the mass density. Equation 3.2 is used to advance the momentum of the fluid. Finally the advective term of equation 3.3, the induction equation, is advanced. This is done by integrating the equations using a finite volume method which is second order accurate in space and time. In order to achieve second order spatial and temporal accuracy the fluxes of a piecewise constant solution at time=t^n are calculated for $\rho_1, \mathbf{v}_1$ and P_1 using a Riemann solver. These fluxes are then used to find a set of fluxes of second order spatial and temporal accuracy by using a time centred solution which

can be reconstructed, using non-linear averaging of the gradients, into a second order piecewise linear solution.

2. The densities and velocities of the charged species are advanced. The continuity equation, equation 3.1, advances the densities of the charged species. The velocities of the charged species are then found analytically. Firstly, the current density is determined using equation 3.6 which can then be used to determine the electric field by using the generalised Ohm's law, 1.91. The momentum equation, equation 3.4, may be re-written in the reference frame of the neutral fluid and is given by;

$$\mathbf{v'}_i \times \mathbf{B} - \frac{\rho_1 K_{i1} \mathbf{v'}_i}{\alpha_i} = \mathbf{E'} \tag{3.10}$$

where,$\mathbf{v}_i$ are the velocities of the charge fluids in the reference frame of the neutral fluid. If it is assumed that the collisional coefficients are constant the charged velocities are then given by;

$$\mathbf{v'}_i = -\mathbf{A}_i^{-1} \mathbf{E'} \tag{3.11}$$

where $\mathbf{A}_i$ is the matrix defined as;

$$\begin{bmatrix} -K_i & B_z & -B_y \\ -B_z & -K_i & B_x \\ B_y & -B_x & -K_i \end{bmatrix} \tag{3.12}$$

The velocities of the charged species can then be found using;

$$\mathbf{v}_i = \mathbf{v'}_i + \mathbf{v} \tag{3.13}$$

3. The final operation advances the magnetic field. The diffusive term of the induction equation, equation 3.3, is solved. Although, when using standard discretization the time-step gets increasingly small as the values of the Hall resistivity get large (O'Sullivan and Downes, 2006, 2007). The problem of this vanishing time-step is dealt with by a technique known as the Hall Diffusion Scheme developed by O'Sullivan and Downes (2006, 2007) which will be discussed later in this section.

Stability Analysis

As mentioned in the previous section, integrating the diffusive term of the induction equation leads to an increasingly small value for the time step for large Hall resistivities. In order to examine the restrictions imposed on the timestep by the Hall resistivity a stability analysis is carried out following that of O'Sullivan and Downes (2007). First, the hyperbolic flux term of the induction equation, equation 3.3, is dealt with separately leaving the induction equation as;

$$\frac{\partial \mathbf{B}}{\partial t} = -\nabla \times \mathbf{E}' \tag{3.14}$$

where $\mathbf{E}'$ can be written as $\mathbf{E}' = \mathbf{E}_O + \mathbf{E}_A + \mathbf{E}_H$. The R.H.S. of the induction equation can then be expanded as follows;

$$\nabla \times \mathbf{E}_X = \mathbf{F}_X^1 + \mathbf{F}_X^2 \tag{3.15}$$

where the subscript X can be O,H or A, and $\mathbf{F}^1$ and $\mathbf{F}^2$ are linear and second order terms. If it is assumed that Ohmic resistivity is negligible based on the fact that the collisional drag on the charged species is dominated by magnetic forces, the Ohmic terms can be ignored and one is left with the linear and second order terms for the ambipolar and Hall cases. It can also be assumed that only small perturbations about a mean field in $\mathbf{B}$ are present, under this assumption the second order terms can be neglected leaving only the first order term for both the ambipolar and Hall cases as follows;

$$\mathbf{F}_A^1 = [\mathbf{a}_A \cdot [\nabla \times \mathbf{J})]\mathbf{a}_A - [(\mathbf{a}_A \cdot \nabla)\mathbf{J}] \times \mathbf{a}_A \tag{3.16}$$

and,

$$\mathbf{F}_H^1 = (\mathbf{a}_H \cdot \nabla)\mathbf{J} \tag{3.17}$$

where $\mathbf{a}_H = r_H\mathbf{b}$, $\mathbf{a}_A = \sqrt{r_A}\mathbf{b}$ and $\mathbf{b}$ is the unit vector in the direction of the magnetic field.

The induction equation can now be written as;

$$\frac{\partial \mathbf{B}}{\partial t} = -\mathbf{G}\mathbf{B} \tag{3.18}$$

where $\mathbf{G}$ is a matrix operator given by, $\mathbf{G} = \mathbf{G}_A + \mathbf{G}_H$. By using the unit vector $\mathbf{b}$ and the operand $(\cdot)$, $\mathbf{G}_A$ and $\mathbf{G}_H$ can be given as;

$$\mathbf{G}_A = r_A[\mathbf{b} \cdot (\nabla \times (\nabla \times \cdot))]\mathbf{b} - r_A[(\mathbf{b} \cdot \nabla)(\nabla \times \cdot)] \times \mathbf{b} \tag{3.19}$$

$$\mathbf{G}_H = -r_H(\mathbf{b} \cdot \nabla)(\nabla \times \cdot) \tag{3.20}$$

In order to obtain the discretization of the matrix operator $\mathbf{G}$ at time level l the second order derivatives of B must be used, these are given as follows;

$$\left(\frac{\partial^2 \mathbf{B}}{\partial x^2}\right)_i = \frac{B_{i+1} - 2B_i + B_{i-1}}{h^2} \tag{3.21}$$

$$\left(\frac{\partial^2 \mathbf{B}}{\partial x \partial y}\right)_{ij} = \frac{B_{i+1,j+1} - B_{i+1,j-1} - B_{i-1,j+1} + B_{i-1,j-1}}{4h^2} \tag{3.22}$$

In order to carry out the stability analysis a numerical wave is introduced, which is given by;

$$\mathbf{B}^l_{ijk} = B_0 e^{i\omega \cdot \mathbf{i}} \tag{3.23}$$

where, $i \equiv \sqrt{-1}$, $\omega = (\omega_x, \omega_y, \omega_z)$, $\mathbf{B}_0$ is the amplitude of the wave and $\mathbf{i} = (i, j, k)$. Equations 3.21 and 3.22 can now be replaced by using (O'Sullivan and Downes, 2007);

$$\frac{\partial^2}{\partial x^2} \rightarrow \lambda_{xx} \equiv -2(1 - \cos\omega_x) \tag{3.24}$$

$$\frac{\partial^2}{\partial x \partial y} \rightarrow \lambda_{xy} \equiv -\sin\omega_x \sin\omega_y \tag{3.25}$$

A matrix Λ is introduced now whose (x, y) member is given by λ_{xy}. Using the substitutions given by equations 3.24, 3.25, the following matrices can be found;

$$\mathbf{A}_H = \begin{bmatrix} 0 & \zeta_z & -\zeta_y \\ -\zeta_z & 0 & \zeta_x \\ \zeta_y & -\zeta_x & 0 \end{bmatrix} \tag{3.26}$$

and,

$$\mathbf{A}_A = \mathbf{b}\zeta + \zeta\mathbf{b} - tr(\Lambda)\mathbf{b}\mathbf{b} - b^T\zeta\mathbf{I} \tag{3.27}$$

where, $\mathbf{b}\zeta$ is the dyadic formed from b and ζ, and $\zeta = \mathbf{\Lambda} b$

1. *Standard Discretization*: The standard discretization scheme can now

be given as;

$$\mathbf{B}^{l+1} = (\mathbf{I} + \tau \mathbf{G}_H^l - \tau \mathbf{G}_A^l)\mathbf{B}^l \tag{3.28}$$

If the numerical wave introduced previously is inserted, equation 3.28 can be written as;

$$\mathbf{B}^{l+1} = (\mathbf{I} - \alpha r_H \mathbf{A}_H - \alpha r_A \mathbf{A}_A)\mathbf{B}^l \tag{3.29}$$

where, $\alpha = \tau/h^2$.

2. *Hall Dominated*: If $\mathbf{A}_A$ is negligible in equation 3.29 the eigenvalues of the evolution operator $(\mathbf{I}) - \alpha r_H \mathbf{A}_H$ are;

$$\mu_1 = 1 \tag{3.30}$$

and,

$$\mu_{2,3} = 1 \pm i\alpha r_H \zeta \tag{3.31}$$

It is clear from the above equation that for all $\tau > 0$, the spectral radius operator is greater than unity. It is also clear that;

$$\bar{\tau}_H^{STD} \to 0 \text{ as } \eta \to 0 \tag{3.32}$$

So, in cases of systems where Hall resistivity is dominant the standard discretization is very restrictive as the time step becomes vanishingly small for significant values of Hall resistivity. A method to overcome this restriction, known as the Hall Diffusion Scheme, has been developed by O'Sullivan and Downes (2006, 2007). The Hall Diffusion Scheme will be detailed later in this section.

3. *Ambipolar Dominated*: If $\mathbf{A}_H$ is negligible in equation 3.29, as is the case for an ambipolar dominated system, then the eigenvalues for the evolution operator, $(\mathbf{I} - \alpha r_A \mathbf{A}_A)$, are;

$$\mu_1 = 1 + \alpha r_A \mathbf{b}^T \zeta \tag{3.33}$$

and,

$$\mu_{2,3} = 1 + \frac{1}{2}\alpha r_A [tr(\Lambda) \pm |tr(\Lambda)\mathbf{b} - 2\zeta|] \tag{3.34}$$

The spectral radius operator can be found to be at $\omega = \pi(1, 1, 1)$ for an arbitrary magnetic field. Therefore the normalised stability limit is then found to be;

$$\bar{\tau}_A^{STD} \leq \frac{1}{2}\frac{\sqrt{1+\eta^2}}{\eta} \tag{3.35}$$

where $\eta = r_A/|r_H|$ parameterizes the relative importance of ambipolar and Hall resistivities. $\tau^{\perp}$ is the cell crossing time for diffusion in the direction perpendicular to the magnetic field;

$$\tau^{\perp} = \frac{h^2}{2\sqrt{r_H^2 + r_A^2}} \tag{3.36}$$

The time interval is normalised such that $\bar{\tau} \equiv \tau/\tau^{\perp}$

Super Time-Stepping

A method known as "super time-stepping" (STS) may be used when solving parabolic problems in explicit schemes. The STS method may be used to accelerate the timestepping for the ambipolar case outlined above.

The method works by first choosing a time-step $d\tau_j$ so as to relax the normal stability restrictions. A series of N_{STS} sub-steps are then used to build a composite time-step known as a super-step so that;

$$\tau^{STS} = \sum_{j=1}^{N_{STS}} d\tau_j \tag{3.37}$$

The stability limit for the STS method can be found for a time-step limit, $\bar{\tau}_A^{STD}$, as;

$$\lim_{\nu \to 0} \bar{\tau}_A^{STS} \to N_{STS}^2 \bar{\tau}_A^{STS} \tag{3.38}$$

with the method becoming unstable when ν, a damping factor, is zero. Richardson extrapolation is employed in order to make the STS method second order in time (Richardon, 1911). A more detailed discussion of super time-stepping can be found in Alexiades et al. (1996).

Hall Diffusion Scheme

As stated previously, for cases when r_H is large, and the ambipolar term is neglected, the time-step for standard discretization becomes vanishingly small and is therefore unstable. The Hall Diffusion Scheme (HDS)(O'Sullivan and Downes, 2006, 2007) can be used to overcome this instability. The Hall Diffusion Scheme makes use of the skew-symmetric matrix $\mathbf{G}_H^l$, so the reduced induction equation for the Hall dominated case, $\frac{\partial \mathbf{B}}{\partial t} = -\mathbf{G}_H \mathbf{B}$, can be written as a system of equations which describing the magnetic field evolution, these equations are strictly explicit;

$$B_{l+1}^x = B_x^l - \tau(G_{x,y}^l B_y^l + G_{y,z}^l B_z^l) \tag{3.39}$$

$$B_{l+1}^y = B_y^l - \tau(G_{y,z}^l B_z^l + G_{y,x}^l B_x^{l+1}) \tag{3.40}$$

$$B_{l+1}^z = B_z^l - \tau(G_{z,y}^l B_x^{l+1} + G_{z,y}^l B_y^{l+1}) \tag{3.41}$$

The stability properties of HDS come from the fact that the right hand sides of equations, 2.39 and 2.40, contain implicit like terms at time t^{l+1}. The matrix form of HDS may now be written as;

$$\mathbf{B}^{n+1} = (\mathbf{I} - \alpha r_H \hat{\mathbf{k}}\hat{\mathbf{k}}\mathbf{A}_H)(\mathbf{I} - \alpha r_H \hat{\mathbf{j}}\hat{\mathbf{j}}\mathbf{A}_H)(\mathbf{I} - \alpha r_H \hat{\mathbf{i}}\hat{\mathbf{i}}\mathbf{A}_H)\mathbf{B}^n \tag{3.42}$$

where $\hat{\mathbf{i}}\hat{\mathbf{i}}$,$\hat{\mathbf{j}}\hat{\mathbf{j}}$ and $\hat{\mathbf{k}}\hat{\mathbf{k}}$, are dyadics formed from unit vectors $\hat{\mathbf{i}}$,$\hat{\mathbf{j}}$ and $\hat{\mathbf{k}}$ respectively. The eigenvectors for the above evolution operator are found to be;

$$\mu_1 = 1 \tag{3.43}$$

and,

$$\mu_{2,3} = 1 - \frac{1}{2}g \pm \frac{1}{2}\sqrt{g(g-4)} \tag{3.44}$$

Here, $g = (\alpha r_H)^2(\zeta^2 - \alpha r_H \zeta_x \zeta_y \zeta_z)$. It can be seen that in order for the evolution operator to be stable;

$$0 \leq g \leq 4 \tag{3.45}$$

By using the most restrictive conditions such that, $\mathbf{b} = (\frac{1}{\sqrt{3}})(1,1,1)$ and $\omega = (\frac{2\pi}{3})(1,1,1)$ and related points of symmetry, and N_{HDS} sub-steps per

time-step, the stability criterion is found to be;

$$\bar{\tau}_H^{HDS} \leq N_{HDS} \frac{4}{\sqrt{27}} \sqrt{1-\eta^2} \tag{3.46}$$

In order to extend HDS to second order accuracy Richardson extrapolation is used in a similar way to the super time-stepping method.

To integrate both Hall and ambipolar terms a combination of the above schemes is used. In order to find the limit for the stable time-step the minimum of the STS and HDS stable time-steps can be used as follows (O'Sullivan and Downes, 2006, 2007);

$$\bar{\tau}^{STS/HDS} = \begin{cases} \bar{\tau}_H^{HDS} & \text{if } \eta \leq \eta^* \\ \bar{\tau}_A^{STS} & \text{otherwise} \end{cases} \tag{3.47}$$

where η^* is the solution of $\bar{\tau}_H^{HDS} = \bar{\tau}_A^{STS}$

3.1.3 Treatment of Magnetic Divergence

In order to ensure the non-divergence of the magnetic field in the system and avoid the creation of magnetic monopoles some control on the magnetic field is required so that Gauss' Law $\nabla \cdot \mathbf{B} = 0$, holds. In the HYDRA code the method used to control the magnetic field is known as the Dedner method (Dedner et al., 2002). The Dedner method controls the divergence of the magnetic field by damping the errors and advecting them to the boundaries of the domain. The method implements a two-fold approach to the problem, first of all the code uses a parabolic correction term which acts to dissipate and smooth the divergence error. Secondly, a hyperbolic term is implemented which acts to advect the error to the domain boundary, the speed at which

the error is advected is the maximum allowable before additional errors are introduced to the solution. The minimisation of errors is also controlled by ensuring that the ratio of the parabolic and hyperbolic correction terms is constant. For a detailed discussion of the Dedner method and for numerical tests of the method the reader is directed to Dedner et al. (2002).

3.1.4 Shock-Tube Tests

A number of shock-tube tests were carried out on the HYDRA code by O'Sullivan and Downes (2007) in order to check the accuracy of the numerical code. These tests were run at an oblique angle to the coordinate axis of the code, in the $(1, 1, 1)$ direction. Although a grid of dimensions N^3 was allocated for each of the tests, the solution of the problem was calculated within a very narrow beam with a radius of one cell. The length of the beam was finite so that it was fully contained within the computational domain. Cells which are outside of the beam are treated as boundary cells and are referenced by their parallel displacement to the beam. For cells that have a parallel displacement which was outside the range of the beam, these cells were set to a fixed value. For cells within the beam, a reference cell was chosen at each value of parallel displacement from which all external cells of the same value were duplicated. This approach allowed for the use of only a small fraction of the N^3 grid to obtain the solution to the fully 3-Dimensional problem.

The dynamic algorithms of the HYDRA code were tested by O'Sullivan and Downes (2007) against the solutions of steady isothermal multifluid equations which were obtained using an independent code. The initial conditions for each of the following test cases can be found in table 3.1

Case 1: Ambipolar Dominated

In this test the parameters were set as such; $r_O = 2 \times 10^{-12}$,$r_H = 1.16 \times 10^{-5}$ and $r_A = 0.068$ giving $\eta = 5.86 \times 10^3$, so that ambipolar diffusion dominates

Table 3.1: Parameters of the shock tube test cases.(O'Sullivan and Downes, 2007)

Case 1					
Right State	$\rho_1 = 1$	$\mathbf{q_1} = (-1.751, 0, 0)$	$\mathbf{B} = (1, 0.6, 0)$	$\rho_2 = 5 \times 10^{-8}$	$\rho_3 = 1 \times 10^{-3}$
Left State	$\rho_1 = 1.7942$	$\mathbf{q_1} = (-0.9759, -0.6561, 0)$	$\mathbf{B} = (1, 1.74885, 0)$	$\rho_2 = 8.9712 \times 10^{-8}$	$\rho_3 = 1.7942 \times 10^{-3}$
	$\alpha_2 = -2 \times 10^{12}$	$\alpha_3 = 1 \times 10^{8}$	$K_{21} = 4 \times 10^{5}$	$K_{31} = 2 \times 10^{4}$	$a = 0.1$
	$\nu = 0.05$	$N_{STS} = 5$	$N_{HDS} = 0$		
Case 2					
Right State	$\rho_1 = 1$	$\mathbf{q_1} = (-1.751, 0, 0)$	$\mathbf{B} = (1, 0.6, 0)$	$\rho_2 = 5 \times 10^{-8}$	$\rho_3 = 1 \times 10^{-3}$
Left State	$\rho_1 = 1.7942$	$\mathbf{q_1} = (-0.9759, -0.6561, 0)$	$\mathbf{B} = (1, 1.74885, 0)$	$\rho_2 = 8.9712 \times 10^{-8}$	$\rho_3 = 1.7942 \times 10^{-3}$
	$\alpha_2 = -2 \times 10^{9}$	$\alpha_3 = 1 \times 10^{5}$	$K_{21} = 4 \times 10^{2}$	$K_{31} = 2.5 \times 10^{6}$	$a = 0.1$
	$\nu = 0$	$N_{STS} = 1$	$N_{HDS} = 8$		
Case 3					
Right State	$\rho_1 = 1$	$\mathbf{q_1} = (-6.7202, 0, 0)$	$\mathbf{B} = (1, 0.6, 0)$	$\rho_2 = 5 \times 10^{-8}$	$\rho_3 = 1 \times 10^{-3}$
Left State	$\rho_1 = 10.421$	$\mathbf{q_1} = (-0.6449, -1.0934, 0)$	$\mathbf{B} = (1, 1.79481, 0)$	$\rho_2 = 5.2104 \times 10^{-7}$	$\rho_3 = 1.00421 \times 10^{-2}$
	$\alpha_2 = -2 \times 10^{12}$	$\alpha_3 = 1 \times 10^{8}$	$K_{21} = 4 \times 10^{5}$	$K_{31} = 2 \times 10^{4}$	$a = 1$
	$\nu = 0.05$	$N_{STS} = 15$	$N_{HDS} = 0$		

the solution.

Using the following equation;

$$\bar{\tau}_A^{STS} = \bar{\tau}_A^{STD} \frac{N}{2\sqrt{\nu}} \frac{\left(1+\sqrt{\nu}\right)^{2N} - \left(1-\sqrt{\nu}\right)^{2N}}{\left(1+\sqrt{\nu}\right)^{2N} + \left(1-\sqrt{\nu}\right)^{2N}} \tag{3.48}$$

it can be estimated that there will be an overall speed up of about a factor of 2 when compared with the standard explicit approach.

The x-component of the neutral velocity field and the y-component of the magnetic field can be seen in figure 3.1 for both the dynamic and steady-state solutions. It can clearly be seen that there was very good agreement between the two solutions. Due to the fact that the HYDRA code is designed to be second-order in space and time, a comparison between the convergence rate of the dynamic solution and the steady-state solution was carried out. This comparison was done using the L1 error norm, e_1, between a section of the two solutions. The section $x_L \leq x \leq x_R$ was fixed about a point x^* when working from the downstream direction. x^* denotes the point where the deviation from the downstream state exceeded 1% of the maximum value of the solution for the first time. By using $x_L = x^* - 0.2$ and $x_R = x^* + 0.8$ it was

found that $e_1 = 1.0 \times 10^{-5}$ for $h = 5 \times 10^{-3}$ and $e_1 = 9.41^{-5}$ for $h = 10^{-2}$. Thus, $e_1 \propto h^{3.2}$, which is above the expected second order convergence. A possible reason for this is the cross-term cancellation which arises from the symmetry of the $(1, 1, 1)$ choice for the variation direction for this problem.

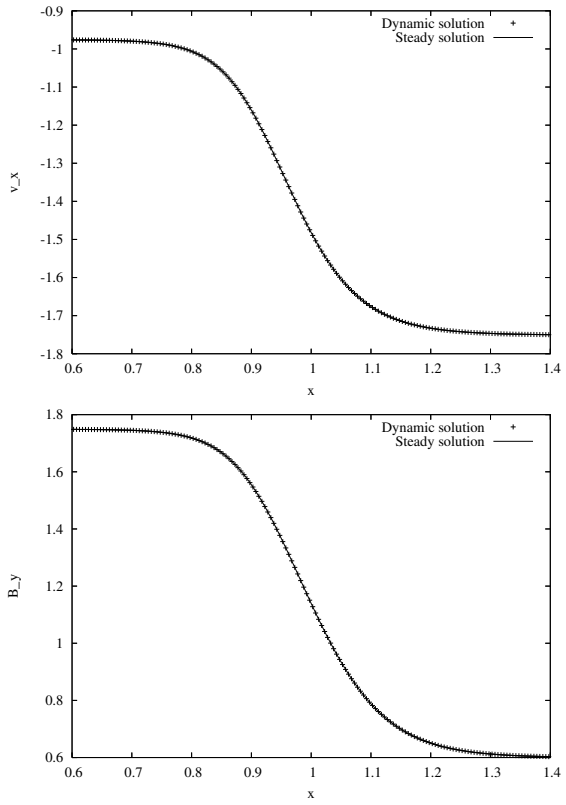

Figure 3.1: The y-component of the magnetic field is shown as well as the x-component of the neutral fluid velocity for case 1 at $h = 5 \times 10^{-3}$ the solution from the dynamic code is shown as points. The overplotted line shows the solution of the steady state equations.(Images taken from O'Sullivan and Downes (2007))

Case 2: Hall Dominated

In this test the Hall term dominated so that the overall efficiency of the scheme was determined by the Hall Diffusion Scheme. As such the parameters for this test were set as follows; $r_O = 2 \times 10^{-9}$, $r_A = 5.44 \times 10^{-4}$, $r_H = 0.0116$ and $\eta = 0.046 \ll 1$[3]. Using the equations;

$$\bar{\tau}^{STD} \leq \frac{8}{9}\frac{\eta}{\sqrt{1+\eta^2}} \tag{3.49}$$

and

$$\bar{\tau}_H^{HDS} \leq N_{HDS}\frac{4}{\sqrt{27}}\sqrt{1+\eta^2} \tag{3.50}$$

it was estimated that the scheme is ≈ 20 times faster than the standard explicit case. The results of the calculations of this test are shown in figure 3.2, with $h = 2 \times 10^{-3}$. For standard explicit schemes the choice of parameters would lead to restrictions on the timestep which would prove prohibitive to the calculation. The use of the Hall Diffusion Scheme allowed the timestep to remain close to the Courant limit which is imposed by the hyperbolic terms throughout the calculations. The characteristics of second order convergence were tested for in the dynamic solution in a similar way to case 1. x^8 denotes the point where the solution deviated 10% from the downstream state. Using $x_L = x^* - 0.05$ and $x_R = x^* + 1.0$, it was found that $e_1 = 5.11 \times 10^{-3}$ for $h = 2 \times 10^{-3}$ and $e_1 = 1.83 \times 10^{-2}$ for $h = 4 \times 10^{-3}$, thus, $e_1 \propto h^{1.8}$. In this case the deviation from the expected second order convergence was attributed to post-shock noise in the high resolution run.

Case 3: Neutral Sub-Shock

The set-up of this test was similar to that of case 1, however in this case there was a higher sound speed and upstream fast Mach number. This set up resulted in a sub-shock developing in the neutral flow due to the interactions between the neutral particles and the charged particles not being strong enough to completely smooth out the initial discontinuity in the neutral flow. This allowed for the testing of the algorithm's ability to deal with discontinuities. As with case 1, it was expected that there was an overall speed up

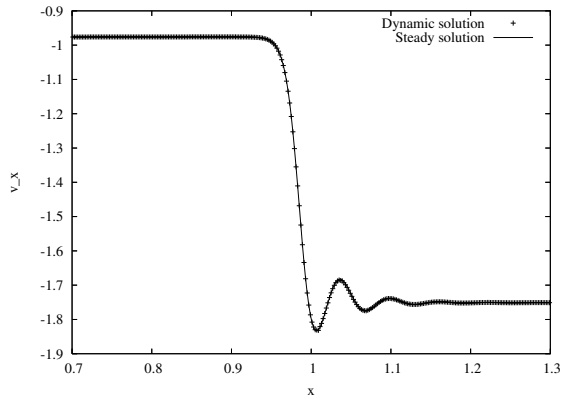

Figure 3.2: The x-component of the neutral fluid velocity for case 2 at $h = 2 \times 10^{-3}$ the solution from the dynamic code is shown as points. The overplotted line shows the solution of the steady state equations.(Images taken from O'Sullivan and Downes (2007))

of a factor of 2, when compared to the standard explicit approach.

The results for the calculations with $h = 1 \times 10^{-3}$ are shown in figure 3.3. It can be seen clearly by the the presence of a discontinuity in u_1 that a sub-shock has developed in the neutral flow, whereas there is no such discontinuity in B_y. A plot of the x-component of the velocity of the negatively charged particles can be seen in figure 3.4, again, there is no discontinuity present in the variable, however, there are some oscillations at the point where the discontinuity occurs in the neutral flow.

Due to the fact that a discontinuity is present in this test and a MUSCL-type scheme was used it was expected that the rate of convergence of the dynamic solution would be first order. Using $x_l = x^* - 0.02$ and $x_R = x^* + 0.1$, where in this case x^* is the point at which the solution deviated from the downstream state by 1%, it was found that $e_1 = 6.44 \times 10^{-3}$ for $h = 1 \times 10^{-3}$ and $e_1 = 1.16 \times 10^{-2}$ for $h = 2 \times 10^{-}3$ therefore, $e_1 \propto h^{0.85}$ which as expected was close to first order. It was suggested that the deviation from first order was due to an error in the charged velocities caused by a discontinuity in the electric field at the sub-shock. It was found that convergence is improved by smoothing the solution with artificial viscosity (O'Sullivan and Downes,

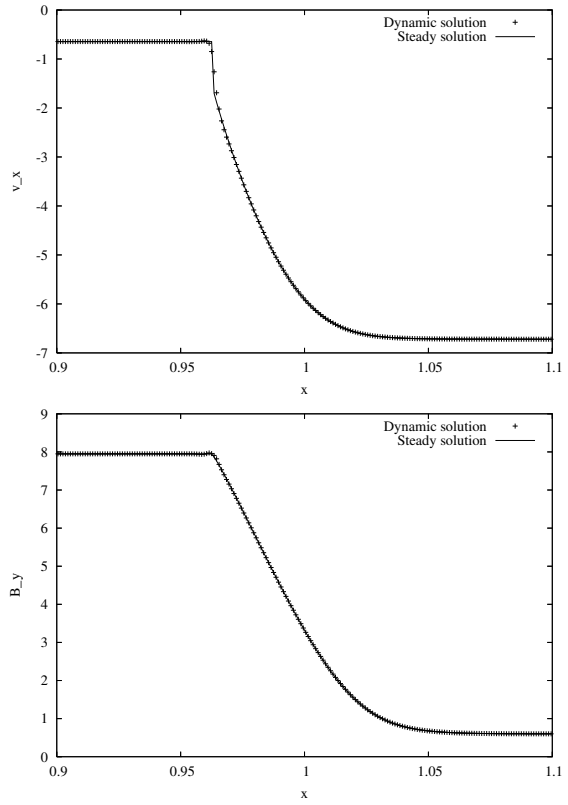

Figure 3.3: The y-component of the magnetic field is shown as well as the x-component of the neutral fluid velocity for case 3 at $h = 1 \times 10^{-3}$ the solution from the dynamic code is shown as points. The overplotted line shows the solution of the steady state equations.(Images taken from O'Sullivan and Downes (2007))

2007).

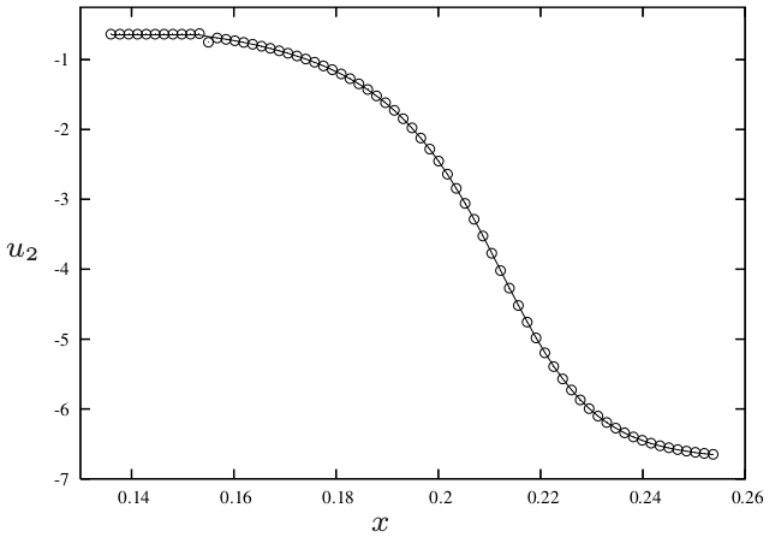

Figure 3.4: The x-component of the negatively charged fluid species is shown at $h = 1 \times 10^{-3}$. The solution from the dynamic code is shown as points. The overplotted line shows the solution of the steady state equations.(Image taken from O'Sullivan and Downes (2007))

Chapter 4

Results and Discussion

The result of a number of simulations of MHD turbulent simulations are presented in this chapter. The length-scales of dissipation structures present in multi-fluid MHD simulations will be analysed. The evolution of the statistics of these structures will also be examined over a significant fraction of the average lifespan of the cloud. An analysis of dissipation structure will also be carried out for an ideal MHD simulation so as to observe the effects of multifluid processes on the formation of dissipation structures. For all of the following simulations the variable being observed is the current density, this is to identify current sheets which are known to dissipate large amounts of energy. As current sheets result from topological changes to the magnetic field, they act to dissipate the energy stored in the magnetic field as thermal energy, through a number of processes which were discussed in section 2.2.2. By choosing to examine the current density, the findings of this work can be compared to those of Zhdankin et al. (2014) which also identify structures in the current density.

4.1 Simulation Set-up

In order to run a simulation which enables the study of MHD turbulence in molecular clouds a set-up file must be created detailing the initial conditions

of the system. This study focuses on driven, isothermal, multifluid MHD systems using the initial conditions given in Downes (2012), and is outlined in the following section.

4.1.1 Initial Conditions

The simulations of multifluid MHD turbulence are run on a uniform Cartesian grid made of $N_x \times N_y \times N_z$ points so that $N_x = N_y = N_z$. The density of the fluid is initially set to $10^4 cm^{-3}$ across the domain. A uniform magnetic field with a strength of $20\mu G$ is applied. The isothermal sound speed was set at a value which corresponds to a temperature of 10K, a reasonable assumption for a molecular cloud, which is $1.88 \times 10^4 cms^{-1}$. The initial velocity of the fluid species is set to zero. The length of the sides of the computational domain are set to be 0.2 pc, so the phenomena observed are indicative of those occurring within the interior of a larger molecular cloud. The charged species are set to have the following properties; The density of the metal ions is $1.27 \times 10^{-25} \mathrm{g} cm^3$ with an average mass of $24 m_p$, where m_p is the proton mass. The metal ions are also assumed to be singly ionised. As one of the assumptions made when creating the model was charge neutrality, the electron density is set accordingly. The resulting ionisation fraction $\xi = n_i/n_n \approx 3 \times 10^{-7}$. The turbulence in the simulations in this study is driven, and so at each time-step velocity increments are added to the velocity of the neutral fluid. This is done by defining the incremental velocity field $\delta\mathbf{u}$. The components of this incremental velocity field are generated from a set of waves with wavenumbers, $k = |\mathbf{k}|$, $3 \leq k \leq 4$. These velocity waves have an amplitude drawn from a Gaussian random distribution of which the mean is 1.0 and the standard deviation is 0.33 and phases between 0 and 2π which are drawn from a uniform distribution. The choice of waves is such that the driving is solenoidal. The addition of these velocity increments simulate the stirring up of the molecular cloud by an external driving force such as stellar winds, etc. The injection rate of energy into the system is given by; $\frac{\dot{E}}{\rho_0 L^2 a^3} = 200$ so that the RMS Mach number and the Alfvénic Mach number are around 4.5 and 3.5 respectively.

4.2 Ideal MHD Turbulence

In this section the simulations results being analysed were created using the initial conditions provided in the previous section of this thesis. The plasma is set to comprise only the neutral fluid and as such the following simulations and results are of Ideal MHD. The number of grid points, or resolution, of the simulation is 256^3

4.2.1 Evolution of Ideal MHD Turbulence

In order to look at the evolution of ideal MHD Turbulence over the course of the simulation four snapshots are taken of the current density. These snapshots are taken at various times during the evolution of the turbulence in the molecular cloud. Figure 4.1 shows these four states, it can be seen that as time progresses the dissipative structures resulting from the turbulence evolve. Figure 4.1a shows the dissipative structures formed during the early stages of the simulation, at $t = 0.035t_c$, it can be seen that the simulation is dominated by large-scale structures. These large structures are produced as a result of the driving mechanism used by the HYDRA code. The turbulence in the simulation is produced by the addition of random perturbations to the velocity field of the neutral fluid as described previously in section 4.1. As the neutral fluid is tied to the magnetic field lines due to the "frozen-in" approximation these perturbations act to change the topology of the magnetic field, causing it to compress in some areas and rarefy in others. The amplitude of the initial driving is a fraction of the simulation domain $\approx 0.05pc$. Therefore, the structures formed at the beginning of the simulation show the length-scale at which energy is injected into the system since the turbulent cascade hasn't had a chance to transfer energy to smaller structures. Figures 4.1b and 4.1c show the dissipative structures formed at $t = 0.07t_c$ and $t = 0.11t_c$ respectively, it can be seen that as the turbulence evolves smaller and smaller scale structures begin to emerge in the simulation. At $t = 0.3t_c$ (when the turbulence was in a statistical steady state, that is, when the energy distribution rate does not vary significantly with respect to time. This

can be seen in figure 4.2 where at later times in the simulation alpha fluctuates very little.), the domain is no longer dominated by large scale structures as can be seen in figure 4.1d. Instead the energy which had been stored in those large structures has be transferred to structures of smaller and smaller scales, until the energy is dissipated at the smallest scales by Ohmic heating, through the current sheets observed and by viscous forces, such as friction between fluid elements in the plasma which causes energy loss through heat.

The evolution of ideal MHD turbulence can also be examined quantitatively. In order to do this the probability distribution of the energy dissipation for each simulation output is calculated. Each of these outputs is assumed to be a power-law similar to that observed in Section 4.2.3. The power-law indices (α) describes the lengths at which energy is dissipated from the system by plotting α over time it is possible to examine the evolution of structures formed as a result of the turbulence, this can be seen in figure 4.2 where α is plotted over the early stages of the simulation (figure 4.2a) and at later times in the simulation (figure 4.2b). It can be seen in figure 4.2a that at early times in the simulation $\alpha > 0$ indicating that the turbulent system is dominated by large scale structures. The peak at the beginning figure 4.2a is due to the driving of the turbulence, since the simulation is in its early stages the energy hasn't has a chance to cascade to smaller length-scales and as such, the structures formed as a result of the driving get larger in size. As time progresses it can be seen in figure 4.2b that $\alpha \to -2.0$ this shows that over time smaller and smaller scale structures are created as energy is transferred through the turbulent cascade. The process by which the power-law indices are calculated will be detailed in the following section.

4.2.2 Dissipative Structure Identification

The identification of structures such as shocks, current sheet and other regions associated with energy dissipation is an important tool in the study of magnetohydrodynamic systems such as turbulent molecular clouds as is the

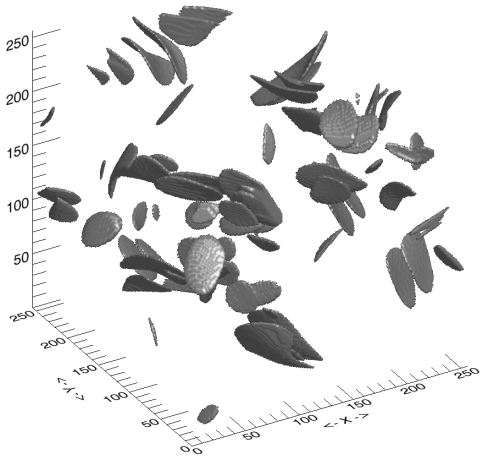

(a) Dissipative structures at $t = 0.035t_c$.

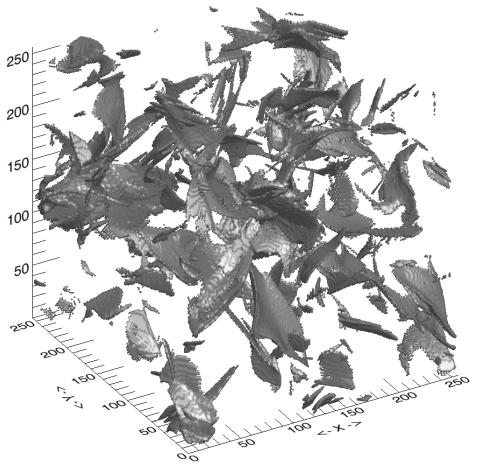

(b) Dissipative structures at $t = 0.07t_c$.

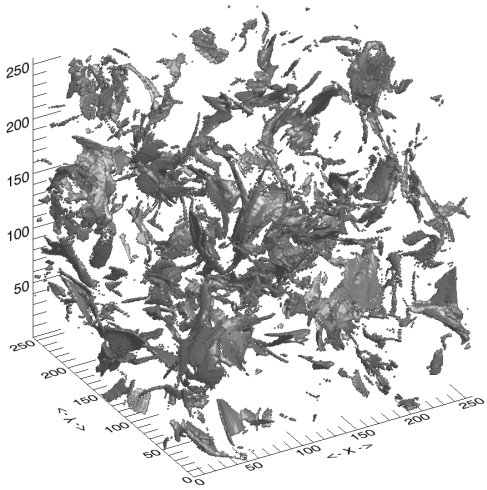

(c) Dissipative structures at $t = 0.11t_c$.

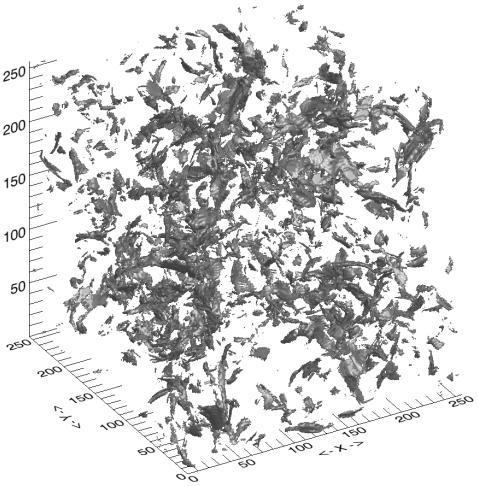

(d) Dissipative structures at $t = 0.3t_c$.

Figure 4.1: Evolution of Ideal MHD dissipative structures.

focus of this study. In order to identify and analyse the statistics of dissipative structures a script was developed for this project called "Euclidean scales". The code developed for this study first identifies regions of interest within the simulation data, the length-scale of this region is then calculated, finally the code calculates statistics based on the length-scales of the regions. The details of the code will be discussed in the following sections.

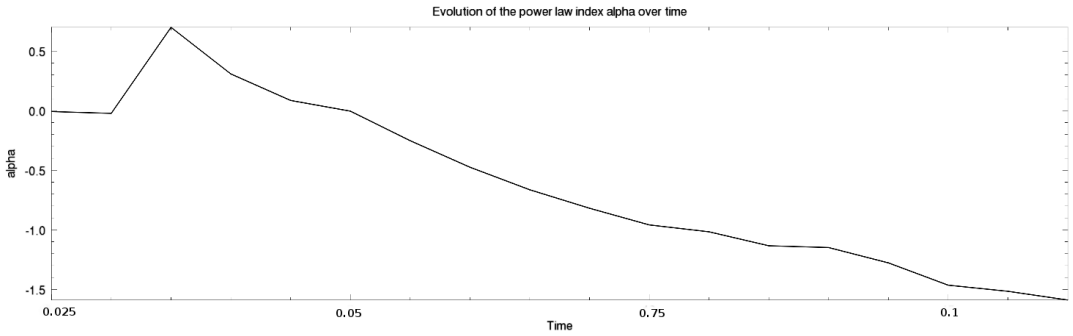

(a) Evolution of the power-law index over $t = [0.025, 0.11]$ sound crossing times.

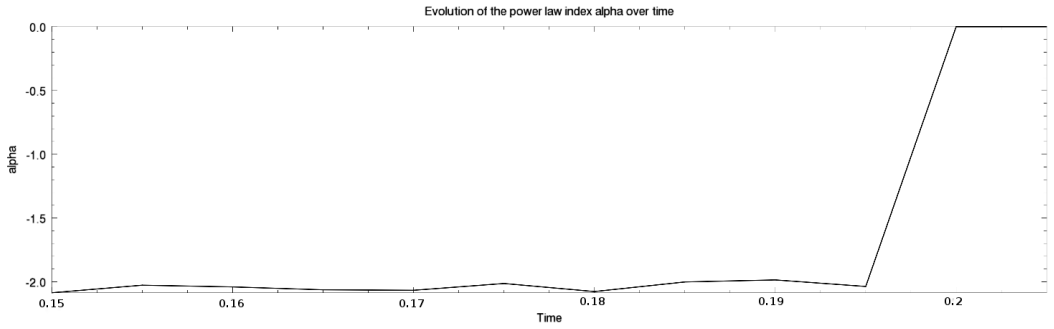

(b) Evolution of the power-law index over $t = [0.15, 0.25]$ sound crossing times.

Figure 4.2: Evolution of the power-law index over time at the start of the simulation (a) and when the simulation had reached a statistical steady state (b) for the case of ideal MHD turbulence. It can be seen that although the initial driving of the turbulence creates large scale structures, the turbulent energy cascade dissipates energy into smaller scale structures.

Identification of Dissipative Regions

In order to identify structures associated with dissipative regions the following steps are implemented;

1. Assuming that a data file has been read into IDL the first step in identifying dissipative structures is to find regions where the value of the variable of interest is greater than a user defined threshold. A binary image of these regions is then created.

2. Using the binary image containing isolated regions, it is then possible to label these regions using the "LABEL_REGION" function in IDL so that they are treated as unique regions in later processes. An array can then be created using the histogram function which contains the number of pixels or volume contained in each region.

3. Once an array has been created containing the volume of each region, it is then possible to count the number of regions with volumes above a specified volume. This is done to ensure that structures containing only a few pixels are ignored as they may introduce errors later in the code.

Once the number of structures and their corresponding volumes have been obtained the length-scales of the structures can be found and used to create an array containing the number of structures and their length. The details of the calculation of the lengths of the structures are given in the following section.

Calculation of Structure Length-Scale

We define the length of a structure as the maximum distance between any two points in that structure. The script finds the maximum distance between any two points in the following way;

- First, a loop is implemented so that each structure is isolated from other structures. This is done to ensure the following steps can be carried out efficiently.

- If the maximum distance between two points in this structure was to be calculated at this stage it would be computationally expensive and

would take a considerable period of time to complete. To avoid unnecessary waiting times, the structure is reduced to just the outer shell of pixels. To obtain the "shell" of the structure, a 3×3 structural element(mask) is created. The structure is eroded, the pixels of the outside edge are removed, this eroded image is then subtracted from the original structure so that only a shell of pixels remains. This leaves us with considerably less points which need to have their distances calculate. This drastically cuts down the computing time for the following step.

- The distance from each point to every other point in the shell is calculated and the maximum of these distances is then taken as the length of the structure.

The length of each structure is fed into an array so a histogram can be created which is then used to create a log-log plot of the number of structures against the length scales of the structures.

Finally, a separate script was written in order to automate the above steps by allowing the user to select a database of data files and have the code open, read and calculate the information discussed above from each file automatically. A time averaged log-log plot is then created from the results obtained.

4.2.3 Dissipation Structures

Figure 4.3 shows a visualisation of the current density near the end of the simulation, when the turbulence has entered a statistical steady state, $t = 0.3t_c$ where t_c is the sound crossing time. The current density can be seen to take the form of sheet-like structures through which energy can be dissipated from the system. The statistical steady state is when the index of the probability distribution of energy dissipation rates stops evolving and converges

although the fluid variables and magnetic field fluctuate randomly due to the turbulent motions. It can be seen that the structures present in the domain seem to be an even distribution of small scale structures and larger scale ones. It can clearly be seen that the structures vary in length and width from small length-scales, to scales which are a considerable fraction of the computational domain. Whereas, the thicknesses of the structures present are much smaller than their length and width this can be seen in figure 4.4, which shows a cross section of the current density at $t = 0.3t_c$. The presence of these structures suggests that energy is being primarily dissipated in thin current sheets similar to the results obtained by Zhdankin et al. (2014).

Using the script outlined in Section 4.2.2, the probability distribution for the rate of energy dissipation in the cloud was obtained and this can be seen in figure 4.5. The probability distribution can be represented by a power-law of the form;

$$N \propto L^{\alpha} \tag{4.1}$$

where, N is the number of dissipative structures and L is the length-scales of those structures.

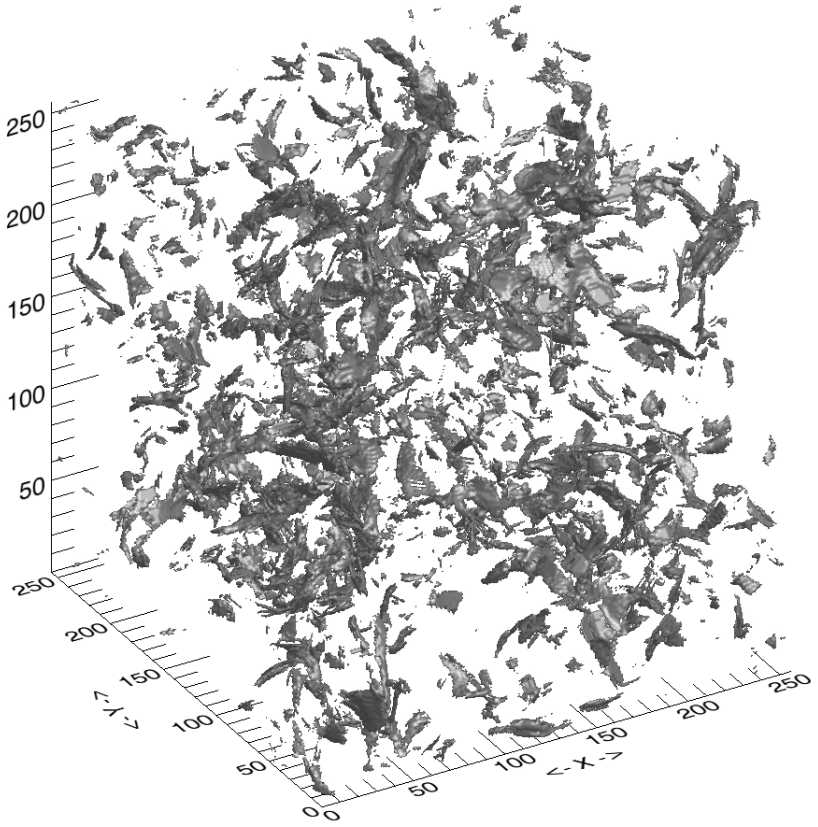

Figure 4.3: Visualisation of the current density at $t = 0.3t_c$ for ideal MHD turbulence. It can be seen that dissipative structures of various length-scales are present.

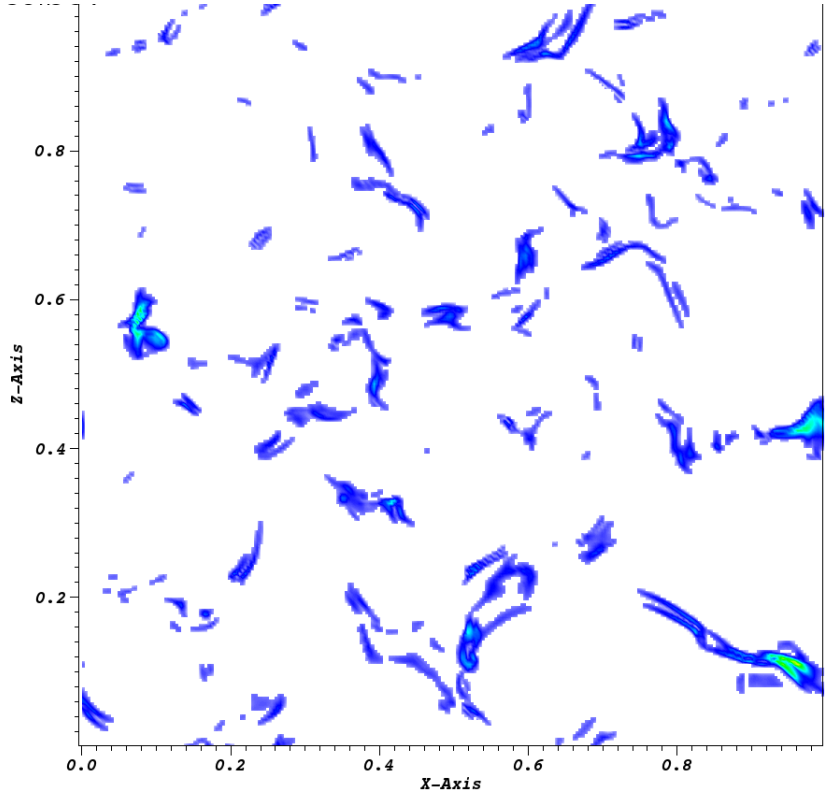

Figure 4.4: Visualisation of the cross-section of the current density in simulation domain for ideal MHD turbulence at $y = 0.5$. A cross-section of the dissipative structures can be seen.

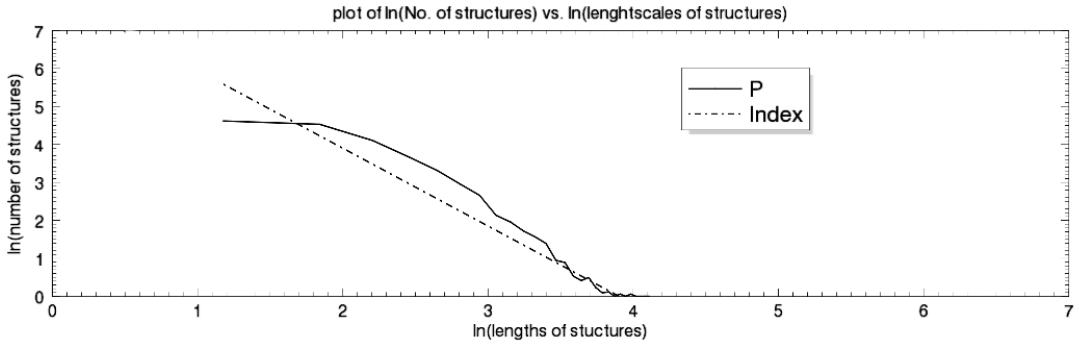

Figure 4.5: Plot of the probability distribution of energy dissipation rates for ideal MHD turbulence which is shown by the solid line (P). The index of this power-law is found to be -2.0. The dot-dashed line (Index) is the straight line fit to the power-law tail of the probability distribution, the slope of which is equal to the power law index

Looking at figure 4.5, it can be seen that the probability distribution exhibits a power-law, with the index of this power-law being -2.0. The index of -2.0 is a critical value indicating that structures of all length-scales contribute equally to the energy dissipation. An index steeper than -2.0 indicates that structures with short length-scales are the dominant source of dissipation, whereas, an index shallower than -2.0 indicates that large scale structures contribute the most to the energy dissipation. The dot-dashed line labelled "Index" in figure 4.5 is the linear fit of the power-law of the probability distribution, the slope of this line is equal to the power-law index of the probability distribution (-2.0). The fact that structures of all length-scales contribute to the dissipation of energy from the system can be explained by the "frozen-in" approximation of ideal MHD. As the magnetic field is tied to the fluid the topology of the field is fixed by the motions of the fluid, as such even when the magnetic field lines get tangled they can remain in that state as they can not undergo magnetic reconnection, this can lead to the formation of very small scale structures with length-scales in the dissipative scale, as well as large scale structures on the driving scale of the system.

4.3 Multifluid MHD Turbulence

Multifluid MHD turbulence will be examined in this section. The initial condition outlined in Chapter 3 are again used to set up the simulation, in a similar fashion to the ideal case above. However, unlike the ideal case, the plasma in the following simulations is comprised of 4 fluids (1 neutral fluid and 3 charged fluids). Thus, multifluid effects will be present and may be important in the formation of dissipation structures.

4.3.1 Dissipation Structures

Figure 4.6 shows a snapshot of the turbulence the structures present at $t = 0.215t_c$. Much like the ideal case these structures appear to span a

range of length-scales, from small structures to larger scale structures. However, unlike in the ideal case it can be seen that there are significantly fewer very small scale structures present. The fact that there are fewer small scale structures present in the multifluid simulation isn't surprising, because if multifluid effects are introduced then diffusive terms are added to the induction equation, equation 3.3. The presence of diffusion, such as ambipolar diffusion, will act to smear out small scale structures. This smearing of small structures by diffusive processes leads to the length-scales associated with these structures increasing, this can be seen if figures 4.3 and 4.6 are compared. The lack of small scale structures in the multifluid simulation indicates that multifluid effects have an impact on the dynamics of MHD turbulence on all scales up to the system scale. This is in contradiction to the observations of Li and Houde (2008), where it was inferred that the multifluid effects were impacting the molecular clouds dynamics at length-scales much less than the driving scale. It can also be seen in figure 4.7 that the thickness of the structures are much less than the length and width of the structures. The fact that the dissipative structures in the presence of ambipolar diffusion are of thickness similar to those observed in the ideal case is in agreement with the work of Brandenburg and Zweibel (1994) and Momferratos et al. (2014) where it is suggested that although ambipolar diffusion on one hand acts to smear out small scale structures, it can also steepen the magnetic field gradients leading to the formation of sharp structures.

The probability distribution of the energy dissipation in the molecular cloud was calculated for the case of multifluid MHD turbulence, which can be seen in figure 4.8.

From figure 4.8 it is shown that the slope of the power-law is shallower than that of the ideal case, $\alpha = -1.02$. This result shows multifluid effects are having an impact on the formation of dissipative structures.

Figure 4.9 shows the evolution of the turbulence in the late stages of the simulation by plotting α against time for $t = [0.1, 0.215]t_c$. It is clear from

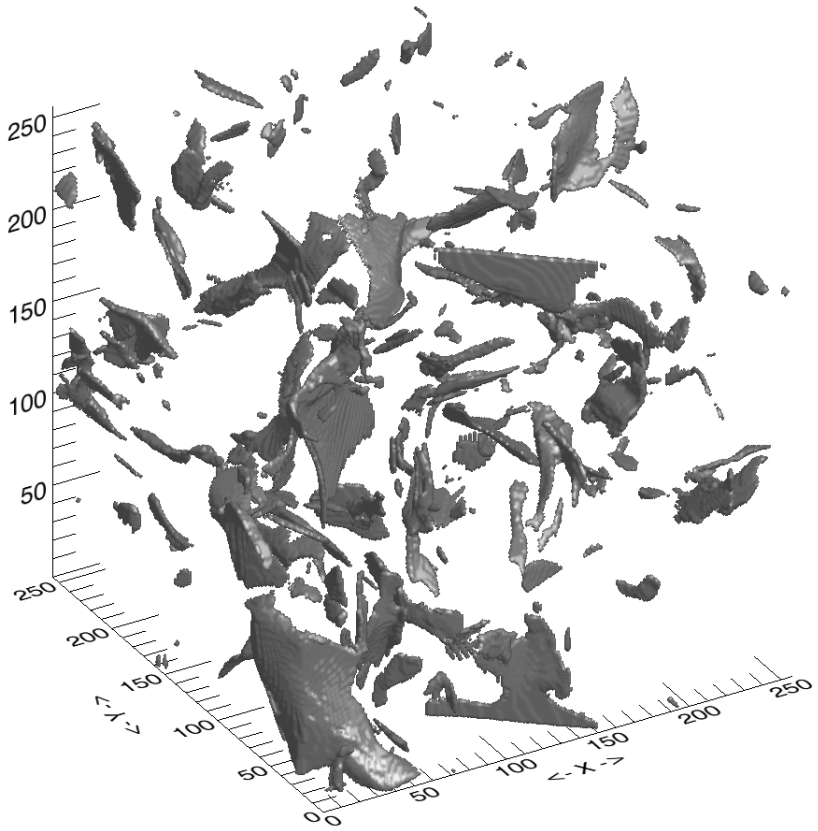

Figure 4.6: Plot of dissipation structures in multifluid MHD turbulence. It can be seen that structures of large length-scales are dominant.

this that the results were obtained when the simulation was in a statistical steady state, with α fluctuating around a value of ~ -1.0. The length-scale of the structures being a result of the initial driving of the plasma can be ruled out because if the turbulence was influenced by the initial driving mechanisms it would be expected that the index of the power-law would not fluctuate around a constant value but, instead, would vary as time progresses. The influence of the initial conditions and driving can be seen in figure 4.10 which shows α plotted over time for the entire duration of the simulation, $t = [0.005, 0.215]$. It is clear that near the beginning of the simulation $\alpha > 0$ indicating that the driving mechanism is creating large scale structures, much like the ideal case, the energy of these structures then cascades to smaller and smaller scales again similar to the ideal case. However, as previously

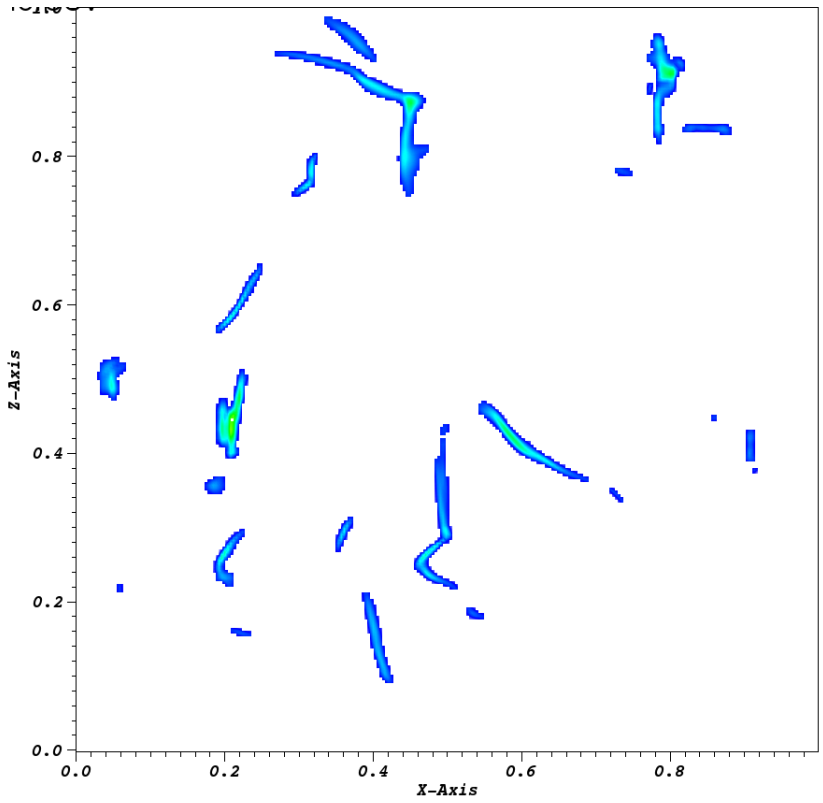

Figure 4.7: Cross-section of the simulation domain for multifluid MHD turbulence at $y = 0.5$. A cross-section of the dissipative structures can be seen.

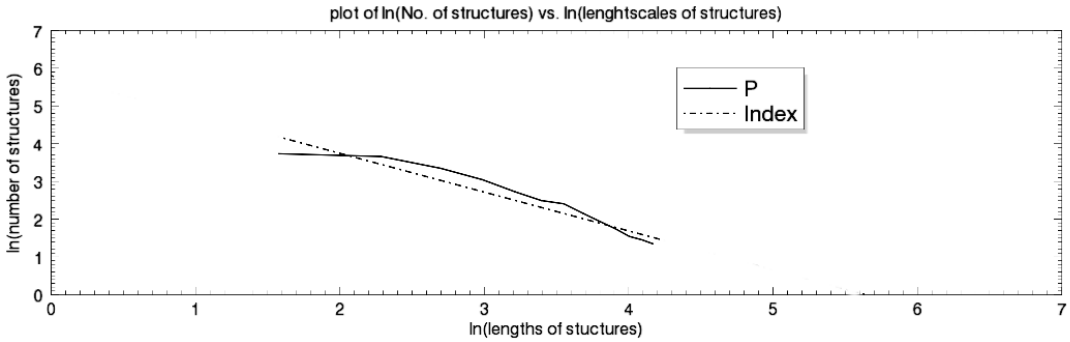

Figure 4.8: Plot of the probability distribution of energy dissipation rates for multifluid MHD turbulence which is shown by the solid line (P) The index of this power-law is found to be -1.02. The dot-dashed line (Index) is the linear fit to the power-law of the probability distribution the slope of which is equal to the power law index (-1.02)

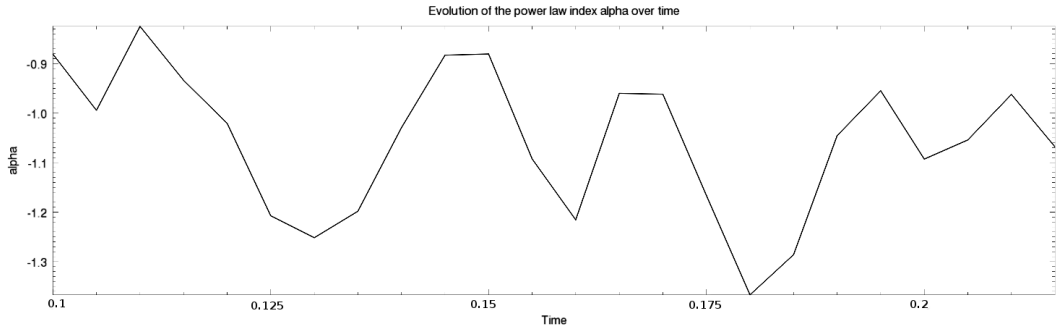

Figure 4.9: Evolution of the power-law index over $t = [0.1, 0.215]$ sound crossing times for multifluid MHD turbulence.

mentioned, unlike the ideal case where $\alpha \to -2.0$, alpha in this case tends to -1.02, that is fewer small scale structures are present.

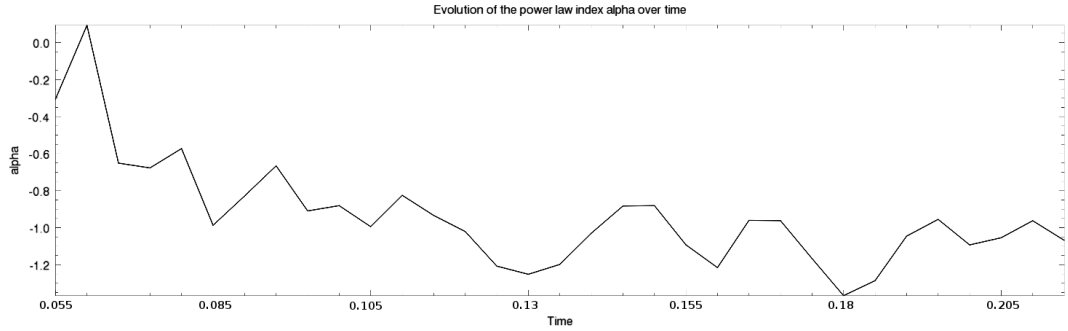

Figure 4.10: Evolution of the power-law index over $t = [0.055, 0.215]$ sound crossing times for multifluid MHD turbulence.

The lack of small scale structures in the multifluid system when compared to the ideal system is in agreement with results presented by Downes (2012). In that work it was found that the presence of multifluid effects acted to smear out most of the small scale structures. Ambipolar diffusion was found to have an impact on the formation of structures in the magnetic field right up to the driving length-scale.

It was seen in the ideal case that due to the "frozen-in" approximation for ideal MHD, the turbulent motions of the plasma resulted in the mag-

netic field being being wound up, that coupled with the fact that under ideal MHD the magnetic field cannot undergo magnetic reconnection allowed for numerous very small scale structures to be formed. However, it can clearly be seen that in the multifluid regime the evolution of the magnetic field, and the dissipation structures which are a result of magnetic field morphology are quite different to that of ideal MHD. The "frozen-in" approximation of ideal MHD breaks down as a result of the inclusion of ambipolar diffusion into the simulation. This allows the magnetic field to decouple from the various plasma fluids and as such it can diffuse through the bulk fluid and allows the magnetic field to evolve differently to the bulk fluid. It then follows that the dissipative structures formed in the multifluid regime will tend to be of larger scale than those in the ideal case as ambipolar diffusion prevents the magnetic field from winding up to the same degree, and as such, fewer small scale structures will be formed.

It should be noted that although the Hall effect is present in these simulations it is not observed to have an impact on the formation of dissipative structures. It would naively be expected that the Hall effect would act to significantly re-orient the magnetic field and as such would result in the presence of a large number of small scale dissipative structures. However work carried out by Jones and Downes (2012) suggests that when ambipolar diffusion is present it inhibits the Hall effect. It is suggested that in a weakly ionised plasma consisting of charged dust grains, an ion fluid, and electron fluid and a neutral fluid, similar to the plasma simulated in this work, the dust grains are coupled to the neutral fluid while the ion and electron fluids are well coupled to the magnetic field lines. The Hall effect is dependent on the current in the system, which in turn depends on the charge densities of the charged species. The charge density of the dust grains is significantly lower than the charge densities of the electron and ion fluids, so the current in the system is then the result of the velocity difference between the ion and the electron fluids which will be relatively small. Therefore the current in the system will mostly be parallel to the magnetic field, resulting in a weak Hall effect. It can be seen in figures 4.7 and 4.6 that the numerous small scale

dissipative structures one would expect due to the Hall effect's twisting of the magnetic field are not present despite the inclusion of the Hall effect in the multifluid simulation, thus the impact of the Hall effect on the formation of dissipative structures is suppressed by ambipolar diffusion.

Chapter 5

Conclusions

This thesis presents a study of ideal and multifluid magnetohydrodynamic turbulence in weakly ionised plasmas such as those found in molecular clouds. Particular attention is paid to the impact of multifluid effects such as ambipolar diffusion and the Hall effect on the formation of dissipative structures in the form of current sheets. The simulations presented in this thesis were carried out using HYDRA, a numerical code which integrates the multifluid MHD equations. Due to the fact HYDRA uses an explicit integration scheme when solving the MHD equations the code is easily parallelized which allows high resolution simulations of multifluid and ideal MHD turbulence to be carried out. The maximum resolution of these simulations depends only on the computational resources available. To the best of the author's knowledge this work presents the first investigation of dissipative structures in the case of a driven, isothermal, fully multifluid MHD turbulent system.

The impact of multifluid effects on the dynamics and evolution of MHD turbulence in molecular clouds is studied by performing both ideal MHD simulations and multifluid MHD simulations comparing the resulting data. This allows us to determine what effect ambipolar diffusion and the Hall effect will have on the formation of dissipative structures in the cloud. It is found that the inclusion of multifluid effects has a significant impact on the evolution of the magnetic field and resulting dissipative system.

The evolution of turbulence and the formation of dissipative current sheets in the ideal MHD case is studied in section 4.2. It is found that the time averaged probability distribution of energy dissipation rates is a power-law with an index of $\alpha = -2.0$ which indicates that in the absence of multifluid effects dissipative structures with lengths and widths which span from the dissipative range right up to scales comparable to the driving scale contribute equally to the dissipation on energy from the system. It is also found that while the length and width of these structures vary considerably, their thickness is quite thin and within the dissipative range. The contribution of thin dissipative structures with lengths and widths spanning the continuum is in agreement with the findings of Zhdankin et al. (2014)

Examining the evolution of the formation of dissipative structures over time it is found that at early times in the simulation of ideal MHD turbulence the length scale of the structures is large, which is expected as the turbulence at this time hasn't developed and as such the energy injected into the system by the driving mechanism cannot be transferred to smaller scales by the turbulent cascade. As time progresses in this simulation the energy is transferred to smaller and smaller scales due to the turbulent energy cascade. The evolution of the ideal MHD turbulence is observed both qualitatively, by visualisation of the turbulence at various times through the simulation, and quantitatively, by plotting the evolution of the power-law index α over time. It is seen that $\alpha \to -2.0$ as time progresses.

In section 4.3 the main aim of this thesis is discussed, that is, the impact of the addition of multifluid effects on the evolution and formation of dissipative structures. It is found that much like the case of ideal MHD turbulence, multifluid MHD turbulence evolves from a state dominated by large-scale dissipative structures resulting from the driving mechanism at early times, to a state where dissipative structures of a variety of length scales are present. However, unlike in the ideal case, when the power-law index α is plotted over time it fluctuates around a value of $\alpha \approx -1.0$ instead of converging to the

value of -2.0 observed in the ideal case. This shallower power law indicates that the presence of multifluid effects in the simulation impacts the formation of dissipative structures such that fewer small scale structures are formed.

The calculation of the time-averaged probability distribution of energy dissipation rates finds that the power-law index for the case of multifluid MHD turbulence is $\alpha = -1.02$, This result indicates that the dissipation of energy from the system is dominated by large scale structures. The visualisation of the dissipative structures formed by multifluid MHD turbulence confirms that far fewer small scale structures are present in the multifluid simulation than are present in the ideal simulation, which is in agreement with the findings of Downes (2012). It is found that the dissipative structures have thicknesses which are similar to the structures formed in the ideal MHD simulation. It is then concluded that the addition of multifluid effects, greatly impacts the formation of dissipative structures in MHD turbulence. Although the thickness of the structures is similar in both the ideal and multifluid cases the presence of ambipolar diffusion smears out small scale dissipative structures, thereby increasing the length scales of these structures.

In conclusion, it was found that the presence of multifluid effects in simulations of MHD turbulence has quite a significant impact on the formation of dissipation structures. The presence of Ambipolar diffusion in particular is the dominant effect governing the evolution of the multifluid simulation acting to diffuse the magnetic field through the bulk fluid, breaking the "frozen-in" approximation of Ideal MHD, thus small structures are smeared out, leaving only larger scale structures. The Hall effect which is included in the multifluid simulation has a negligible impact on the evolution of the turbulence, as ambipolar acts to suppress it through the decoupling of the various fluid species. There is potential for a considerable amount of further work to be carried out. An interesting study which could be performed is to run a series of simulations using the same initial conditions as used in this thesis but varying the importance of the various multifluid effects in each simulation. This would result in ideally a simulation where the Hall effect

dominates, another simulation where Ohmic diffusion dominates and a final simulation where ambipolar diffusion dominates. Having these simulations would allow us to study the impact of the individual multifluid effects on the formation of dissipative structures. This would lead to a greater understanding of the relative importance of the processes on the evolution of turbulence in molecular clouds and therefore on the formation of stars which form in these clouds.

Bibliography

Alexiades, V., Amiez, G. and Gremaud, P.-A. (1996), 'Super-time-stepping acceleration of explicit schemes for parabolic problems', *Communications in Numerical Methods in Engineering* **12**(1), 31–42.
URL: *http://dx.doi.org/10.1002/(SICI)1099-0887(199601)12:1¡31::AID-CNM950¿3.0.CO;2-5*

Berselli, L. (2005), *Mathematics of Large Eddy Simulation of Turbulent Flows, First Edition*, Springer, London.

Binney, J. and Tremaine, S. (2008), *Galactic Dynamics*, Princeton University Press, Princeton.

Blitz, L., Fukui, Y., Kawamura, A., Leroy, A., Mizuno, N. and Rosolowsky, E. (2007), 'Giant Molecular Clouds in Local Group Galaxies', *Protostars and Planets V* pp. 81–96.

Brandenburg, A. and Lazarian, A. (2013), 'Astrophysical Hydromagnetic Turbulence', Space Sci. Rev. **178**, 163–200.

Brandenburg, A. and Zweibel, E. G. (1994), 'The formation of sharp structures by ambipolar diffusion', ApJ **427**, L91–L94.

Carpenter, J. M. and Sanders, D. B. (1998), 'The W51 Giant Molecular Cloud', AJ **116**, 1856–1867.

Ciolek, G. E. and Roberge, W. G. (2002), 'Time-dependent, Multifluid, Magnetohydrodynamic Shock Waves with Grain Dynamics. I. Formulation and Numerical Tests', ApJ **567**, 947–961.

Crutcher, R. M. (1999), 'Magnetic Fields in Molecular Clouds: Observations Confront Theory', ApJ **520**, 706–713.

Crutcher, R. M. (2012), 'Magnetic Fields in Molecular Clouds', ARA&A **50**, 29–63.

Davidson, L. (2011), 'Fluid mechanics, turbulent flow and turbulence modeling', *Chalmers University of Technology, Goteborg, Sweden (Nov 2011)* .

Dedner, A., Kemm, F., Kröner, D., Munz, C.-D., Schnitzer, T. and Wesenberg, M. (2002), 'Hyperbolic Divergence Cleaning for the MHD Equations', *Journal of Computational Physics* **175**, 645–673.

Downes, T. P. (2012), 'Driven multifluid magnetohydrodynamic molecular cloud turbulence', MNRAS **425**, 2277–2286.

Draine, B. T., Roberge, W. G. and Dalgarno, A. (1983), 'Magnetohydrodynamic shock waves in molecular clouds', ApJ **264**, 485–507.

Elmegreen, B. G. (1979), 'Magnetic diffusion and ionization fractions in dense molecular clouds - The role of charged grains', ApJ **232**, 729–739.

Falle, S. A. E. G. (2003), 'A numerical scheme for multifluid magnetohydrodynamics', MNRAS **344**, 1210–1218.

Goldreich, P. and Sridhar, S. (1995), 'Toward a theory of interstellar turbulence. 2: Strong alfvenic turbulence', ApJ **438**, 763–775.

Guelin, M., Langer, W. D., Snell, R. L. and Wootten, H. A. (1977), 'Observations of DCO/plus/ - The electron abundance in dark clouds', ApJ **217**, L165–L168.

Hartmann, L., Ballesteros-Paredes, J. and Bergin, E. A. (2001), 'Rapid Formation of Molecular Clouds and Stars in the Solar Neighborhood', ApJ **562**, 852–868.

Iroshnikov, P. S. (1963), 'Turbulence of a Conducting Fluid in a Strong Magnetic Field', AZh **40**, 742.

Jeans, J. H. (1902), 'The Stability of a Spherical Nebula', *Philosophical Transactions of the Royal Society of London Series A* **199**, 1–53.

Jones, A. C. and Downes, T. P. (2012), 'The Kelvin-Helmholtz instability in weakly ionized plasmas - II. Multifluid effects in molecular clouds', MNRAS **420**, 817–828.

Kolmogorov, A. (1941), 'The Local Structure of Turbulence in Incompressible Viscous Fluid for Very Large Reynolds' Numbers', *Akademiia Nauk SSSR Doklady* **30**, 301–305.

Kraichnan, R. H. and Nagarajan, S. (1967), 'Growth of Turbulent Magnetic Fields', *Physics of Fluids* **10**, 859–870.

Lada, C. J. (1987), Star formation - From OB associations to protostars, *in* M. Peimbert and J. Jugaku, eds, 'Star Forming Regions', Vol. 115 of *IAU Symposium*, pp. 1–17.

Larson, R. B. (2002), Summary: Modes of Star Formation (Invited), *in* E. K. Grebel and W. Brandner, eds, 'Modes of Star Formation and the Origin of Field Populations', Vol. 285 of *Astronomical Society of the Pacific Conference Series*, p. 442.

Levine, R. H. (1974), 'A New Theory of Coronal Heating', ApJ **190**, 457–466.

Li, H.-b. and Houde, M. (2008), 'Probing the Turbulence Dissipation Range and Magnetic Field Strengths in Molecular Clouds', ApJ **677**, 1151–1156.

Mac Low, M.-M. and Klessen, R. S. (2004), 'Control of star formation by supersonic turbulence', *Reviews of Modern Physics* **76**, 125–194.

Momferratos, G., Lesaffre, P., Falgarone, E. and Pineau des Forêts, G. (2014), 'Turbulent energy dissipation and intermittency in ambipolar diffusion magnetohydrodynamics', MNRAS **443**, 86–101.

Mouschovias, T. C. (1976), 'Nonhomologous contraction and equilibria of self-gravitating, magnetic interstellar clouds embedded in an intercloud medium: Star formation. I Formulation of the problem and method of solution', ApJ **206**, 753–767.

Mouschovias, T. C. and Spitzer, Jr., L. (1976), 'Note on the collapse of magnetic interstellar clouds', ApJ **210**, 326.

Myers, P. C. and Ladd, E. F. (1993), 'Bolometric temperatures of young stellar objects', ApJ **413**, L47–L50.

O'Sullivan, S. and Downes, T. P. (2006), Numerical Modeling of Weakly Ionized Plasmas, *in* G. P. Zank and N. V. Pogorelov, eds, 'Numerical Modeling of Space Plasma Flows', Vol. 359 of *Astronomical Society of the Pacific Conference Series*, p. 178.

O'Sullivan, S. and Downes, T. P. (2007), 'A three-dimensional numerical method for modelling weakly ionized plasmas', MNRAS **376**, 1648–1658.

Padmanabhan, T. (2000), *Theoretical Astrophysics. Vol I: Astrophysical Processes*, Cambridge University Press, Cambridge.

Priest, E. (2000), *Solar Magnetohydrodynamics*, Kluwer Academic Publishers, Holland.

Richardon, L. (1911), 'The Approximate Arithmetical Solution by Finite Differences of Physical Problems Involving Differential Equations, with an Application to the Stresses in a Masonry Dam', *Phil. Trans. R. Soc. London, Sec. A* **210**, 307–357.

Sanders, D. B., Scoville, N. Z. and Solomon, P. M. (1985), 'Giant molecular clouds in the Galaxy. II - Characteristics of discrete features', ApJ **289**, 373–387.

Servidio, S., Matthaeus, W. H., Dmitruk, P., Shay, M. A., Cassak, P. and Wan, M. (2010), 'Statistics of magnetic reconnection in two-dimensional magnetohydrodynamic turbulence', *AGU Fall Meeting Abstracts* .

Shebalin, J. V., Matthaeus, W. H. and Montgomery, D. (1983), 'Anisotropy in MHD turbulence due to a mean magnetic field', *Journal of Plasma Physics* **29**, 525–547.

Shore, S. (2003), *The Tapestry of Modern Astrophysics*, John Wiley & Sons, inc., New Jersey.

Shu, F. H., Adams, F. C. and Lizano, S. (1987), 'Star formation in molecular clouds - Observation and theory', ARA&A **25**, 23–81.

Siversky, T. V. and Zharkova, V. V. (2009), 'Particle acceleration in a reconnecting current sheet: PIC simulation', *Journal of Plasma Physics* **75**, 619–636.

Soler, R., Carbonell, M. and Ballester, J. L. (2013), 'Magnetoacoustic Waves in a Partially Ionized Two-fluid Plasma', ApJS **209**, 16.

Tobias, S. M., Cattaneo, F. and Boldyrev, S. (2011), 'MHD Dynamos and Turbulence', *ArXiv e-prints* .

Treumann, R. A. and Baumjohann, W. (2013), 'Collisionless Magnetic Reconnection in Space Plasmas', *Frontiers in Physics* **1**, 31.

Troland, T. H. (2005), Magnetic Field Strengths in the Cold Neutral Medium of the Galaxy, *in* A. Adamson, C. Aspin, C. Davis and T. Fujiyoshi, eds, 'Astronomical Polarimetry: Current Status and Future Directions', Vol. 343 of *Astronomical Society of the Pacific Conference Series*, p. 64.

Tucker, W. H. (1973), 'Heating of Solar Active Regions by Magnetic Energy Dissipation: the Steady-State Case', ApJ **186**, 285–290.

Vekstein, G. and Priest, E. R. (1993), 'Magnetostatic equilibria and current sheets in a sheared magnetic field with an X-point', Sol. Phys. **146**, 119–125.

Young, H. and Freedman, R. (2012), *University Physics with Modern Physics*, Peason Education, London.

Zhdankin, V., Boldyrev, S., Perez, J. C. and Tobias, S. M. (2014), 'Energy Dissipation in Magnetohydrodynamic Turbulence: Coherent Structures or "Nanoflares"?', ApJ **795**, 127.

Zhdankin, V., Uzdensky, D. A. and Boldyrev, S. (2015), 'Temporal Analysis of Dissipative Structures in Magnetohydrodynamic Turbulence', ApJ **811**, 6.